[American Journal of Science, Vol. 320, January, 2020, P. 27–52, DOI 10.2475/01.2020.03]

CRYSTAL SURFACE REACTIVITY ANALYSIS USING A COMBINED APPROACH OF X-RAY MICRO-COMPUTED TOMOGRAPHY AND VERTICAL SCANNING INTERFEROMETRY

WOLF-ACHIM KAHL*,†, TAO YUAN**, TILL BOLLERMANN**, WOLFGANG BACH*,***, and CORNELIUS FISCHER**,†

ABSTRACT. Dissolution rates of porous crystalline materials reflect the superposition of transport and surface control, mainly via the parameters saturation of the ambient fluid and distribution of surface energy. As a result, reacting surfaces evolve over time showing a heterogeneous distribution of surface rates. The spatiotemporal heterogeneity of surface reaction rates is analyzed using the rate map and rate spectra concept. Here, we quantify the dissolution rate variability covering the nm- to mm-scale of dissolving single-crystal and polycrystalline calcite samples, using a combined approach of X-ray micro-computed tomography (μ-CT) and vertical scanning interferometry (VSI). The dissolution experiments cover reaction periods from 15 minutes up to 54 days. The observed rate ranges are remarkably consistent over the entire reaction period but include a variability of about two orders of magnitude ($10^{-9} - 3 \times 10^{-7}$ mol m^{-2} s^{-1}). The rate map data underscore the concurrent and superimposing impact of surface- vs. fluid flow controlled rate portions. The impact of fluid flow on reactivity at the mm-scale in the transport-controlled system is confirmed by 2-D reactive transport modeling. The sub-mm spatial heterogeneity of low vs. high reactivity surface portions of polycrystalline calcite is clearly below the mean crystal size. This suggests the dominant impact of highly reactive surface portions irrespective of the orientation of larger crystals on the overall surface reactivity. Correspondingly, the overall range of intrinsic reactivity heterogeneity as observed using singly crystal material is not further expanded for polycrystalline material. As a general conclusion, numerical reactive transport concepts would benefit from the implementation of a reactivity term resembling the experimentally observed existence of multiple rate components.

Key words: crystal surface reactivity, rate map, dissolution rate variability, X-ray micro-computed tomography (μ-CT), vertical scanning interferometry (VSI), reactive transport, fluid-rock interaction

INTRODUCTION

Reactive transport concepts in complex geomaterials rely on quantitative feedback between fluid flow velocity and surface reactivity via local gradients in fluid saturation (for example, Steefel and others, 2015a; Li and others, 2017; Noiriel and Daval, 2017; Deng and others, 2018). Both components of reactive transport show critical variability and thus affect the spatial heterogeneity of material flux from (dissolution) or to (growth) the reacting material surface. Transport-controlled conditions occur when the concentration in the aqueous phase increases or decreases to the point where equilibrium or near-equilibrium is achieved. Surface-controlled conditions instead apply where the rate of attachment and detachment of ions from the mineral surface is the rate-limiting factor in the overall reaction. The latter factor is often complicated due to small-scale physico-chemical gradients at the reacting interface (for example, Daval and others, 2013; Hellmann and others, 2015; Wild and others, 2016). The competing superimposition of transport-controlled vs. surface-controlled fluid-solid

* Department of Geosciences, University of Bremen, Bremen, Germany
** Helmholtz-Zentrum Dresden-Rossendorf (HZDR), Institut für Ressourcenökologie, Abteilung Reaktiver Transport, Permoserstrasse 15, D-04318 Leipzig, Germany
*** MARUM Center for Marine Environmental Sciences, University of Bremen, Bremen, Germany
† Corresponding authors: wakahl@uni-bremen.de; c.fischer@hzdr.de

interactions is responsible for the complex evolution of porosity and permeability in reacting porous media (for example, Noiriel and Deng, 2018). The heterogeneity of the flow field is controlled by constraints such as tortuosity, permeability, and pore wall roughness (for example, Gouze and Luquot, 2011).

The intrinsic variability of surface reactivity and its spatial distribution is based on factors such as crystal orientation or defect and grain boundary density and distribution (Fischer and others, 2012a; Harries and others, 2013; Pollet-Villard and others, 2016a). During the last two decades, multiple studies utilized atomic force microscopy, vertical scanning interferometry (VSI), and related surface microscopic techniques to quantify the variability of surface reactivity of single-crystal surfaces. This research has been driven by the analysis of well-defined surface features such as etch pits at defect structures, surface steps, and crystal edges with high kink site densities (for example, Pollet-Villard and others, 2016b; Brand and others, 2017; Saldi and others, 2017; Fischer and Luttge, 2018; Noiriel and Daval, 2017; Noiriel and others, 2019). Investigations focusing on contrasting surface reactivity at larger scales showed the critical impact of surface features that develop during long-term reactions, thus implying their impact on the formation of porosity pattern in rocks (for example, Noiriel and others, 2009; Emmanuel and Levenson, 2014; Fischer and Luttge, 2017). On the other hand, several studies integrating true 3-D spatially resolved tomographic data (for example, computed microtomography μ-CT, positron-emission tomography) underscored the critical impact of flow field heterogeneity at the pore scale and above (Berg and others, 2013; Menke and others, 2015; Molins, 2015; Bultreys and others, 2016; Deng and others, 2018; Kulenkampff and others, 2018). 3-D imaging of calcite growth by using time-lapse CT techniques illustrated the flow path alteration due to calcite precipitates (Godinho and Withers, 2018).

Our experimental approach allows for a quantitative insight over a large range of both temporal and spatial scales, a strategy discussed in detail by Noiriel and Daval (2017). We use a combined approach of VSI and X-ray μ-CT in order to quantify the dissolution rate variability at the pore scale, covering the nm- to mm-scale of dissolving single-crystal and polycrystalline calcite samples. Usually, μ-CT is employed to characterize the effective material loss during reaction time by localization of differences in cross-sectional images between initial (prior to experiment) and final state of an experiment, or by quantification of changes in surface area of the segmented mineral- or rather: pore space-models (Noiriel and others, 2005; Noiriel and others, 2009; Smith and others, 2013b; Menke and others, 2015; Pereira Nunes and others, 2016b; Menke and others, 2018; Noiriel and others, 2019; Yuan and others, 2019a). While other tomography methods such as FIB-SEM shift the level of detail into the nm-range (Bera and others, 2011; Hemes and others, 2015; Peuble and others, 2018), their destructiveness precludes comparison of pre- and post reaction states.

In this study, μ-CT and VSI techniques are joint in a novel and complementary approach to quantify the dissolution rate variability covering the nm- to mm-scale of dissolving single-crystal and polycrystalline calcite samples. Initial and final reaction states of the samples in each experiment were either scanned by VSI or X-ray μ-CT. Subsequent to method-dependent quantitative image analysis, the spatially resolved surface retreat on both nanometer and micrometer scale was available for further evaluation. In either method, the mineral surface was ascertained by a surface model for both initial and final reaction states, and the reaction rate was determined locally by division of surface retreat by reaction time. While a number of μ-CT studies recorded porosity gain, permeability change, or pore space evolution in general during percolation experiments (Luquot and Gouze, 2009; Noiriel and others, 2009; Gouze and Luquot, 2011; Sell and others, 2013; Smith and others, 2013b; Smith and others, 2013c; Vialle and others, 2014), in our setup the local advective conditions and flow field

heterogeneity remained basically constant during reaction time. A simple, yet effective flow path geometry for the μ-CT experiment avoids transport complexity introduced by a complex pore network topology, tortuosity, self-diffusivity, *et cetera*. This facilitates a straightforward and obvious data fusion with VSI experiments run with flat calcite cleavages and cut polycrystalline surfaces. Thus, our experimental approach allows for a quantitative insight over a large range of both temporal and spatial scales, gained by two different experimental setups for μ-CT and VSI, both capable of surveillance of surface retreat (either in the range of several nm or μm upon reaction time, respectively). Conceptually, we compare the rate contributors and their temporal evolution in order to decipher the importance of specific rate histogram modes for the long-term evolution of fluid-solid interactions. Both contrasting surface reactivity and the fluid's residence time during reaction are responsible for the local rate distribution. We analyze the impact of crystal orientation (Godinho and others, 2012; Smith and others, 2013a; Godinho and others, 2014; Saldi and others, 2017) by comparing the rate range of well-defined single-crystal (00-14) cleavage plane dissolution vs. the rate range of a multitude of crystal orientations that form the reacting pore wall of a polycrystalline calcite.

Finally, we compare the experimental data with results from reactive transport modeling (RTM). In general, such approaches combine transport calculations based on the geometry of the porous media and chemical calculations of ion concentrations utilizing chemical data from databases (see, for example, Steefel and others, 2015a; Tournassat and Steefel, 2019). Comparison of experimental and numerical approaches at the pore scale of complex porous media provided insight into the heterogeneity of flow velocity and related complex transport-controlled behavior (Flukiger and Bernard, 2009; Molins and others, 2012; Molins and others, 2014; Molins, 2015; Deng and others, 2018; Yuan and others, 2019a). At larger length scales, at the core scale and at reservoir scale the impact of permeability gradients is discussed to be a major controlling factor (Wang and others, 2019).

Important insights about the evolution of reacting systems can be derived from the analysis of pore scale heterogeneity (for example, Molins and others, 2012; Molins and others, 2014; Steefel and others, 2015b), however, current RTM approaches do not address the intrinsic heterogeneity of surface reactivity of reacting materials. Nevertheless, the point of heterogeneity of surface reactivity beside hydraulic and chemical heterogeneity has been raised in the past already and is under discussion for improved upscaling strategies, but remains challenging (for example, Schott and others, 1989; Tartakovsky and others, 2009; Dentz and others, 2011; Berkowitz and others, 2016; Pereira Nunes and others, 2016a; Fischer and others, 2018; Kurganskaya and Churakov, 2018; Noiriel and others, 2019; Yuan and others, 2019a). In this study, the simple geometry of the cylindrical pore in the reacting polycrystalline calcite has been chosen to minimize the complexity of the flow field. Focusing on a simple velocity distribution that can be varied at will allows for a simple deconvolution of the concurrent impact of transport- vs. surface-controlled conditions via the velocity gradient. Thus, any observed dissolution anisotropy of the larger polycrystalline system can be attributed directly to surface- vs. transport-controlled behavior.

MATERIALS AND METHODS

Sample Material

The calcite marble in this study originates from Großsölk (Austria). We used this marble because of its high calcite (95 wt.%) concentration and relative large grain size (mean diameter ~ 500 μm, fig. 1). Accessory minerals are quartz (<2 wt.%), muscovite (<1 wt.%), phlogopite (<1 wt.%) and ore minerals (1< wt.%) (Zeisig and others, 2002). The marble strata is exposed in the southern part of the upper Enns valley and

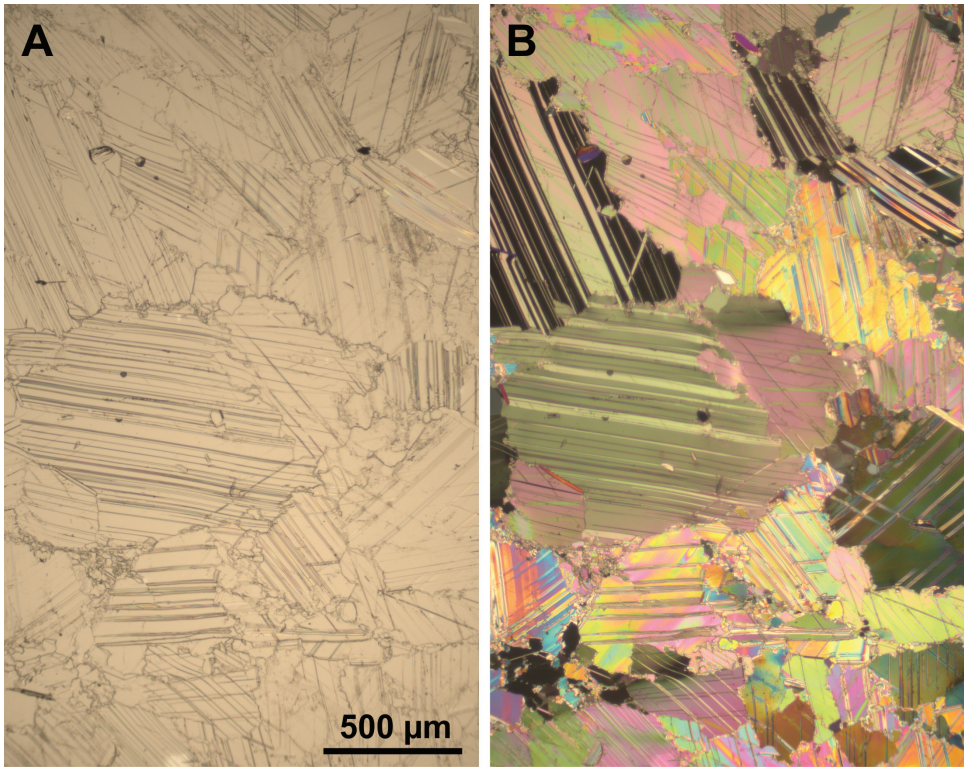

Fig. 1. Thin-section micrographs of the Sölk marble (A: plane-polarized light, B: cross-polarized light).

belongs to the northern part of the Woelzer Glimmerschiefer complex. More details about the so-called Sölk marble from Großsölk is available from the literature (Fritsch, 1953; Zednicek, 1983). The Sölk marble exhibits a marked preferred grain orientation with a uniform direction of calcite c-axis and planar distribution of calcite a-axis. The samples for the µ-CT experiment were prepared to expose relatively uniformly distributed crystal orientations perpendicular c at the drill hole surface. Along the flow path, variations in orientation remain constant, and changes in dissolution rate are independent of changing orientation.

Setup of the Percolation Experiment for µ-CT Surveillance

Marble sample cuboids (fig. 2, I: *ca.* $6 \times 8 \times 9$ mm^3; II: *ca.* $4 \times 8 \times 9$ mm^3) were cut using a microsaw. Subsequently, each specimen was drilled to expose a central hole (Ø *ca.* 1.6 mm). Thereafter, the marble cuboids were cleaned with distilled water in an ultrasonic bath for several minutes to eliminate small particles, potentially produced during the drilling process.

A flow-through experiment was performed for 1292 h (almost 54 days), using the X-ray-transparent PEEK (semicrystalline thermoplastic material; polyether ether ketone) reaction cell setup for rock micro-cores presented by Kahl and others (2016). The samples were mounted within a perforated polyether ether ketone chamber or PEEKin (fig. 2A, outer diameter of 18 mm and an inner diameter of 14 mm). The PEEKin is designed to slot into the PEEK reaction cell setup in place of the rock micro-cores, into which it is shrink-sleeved between the in- and outlet plugs of the core

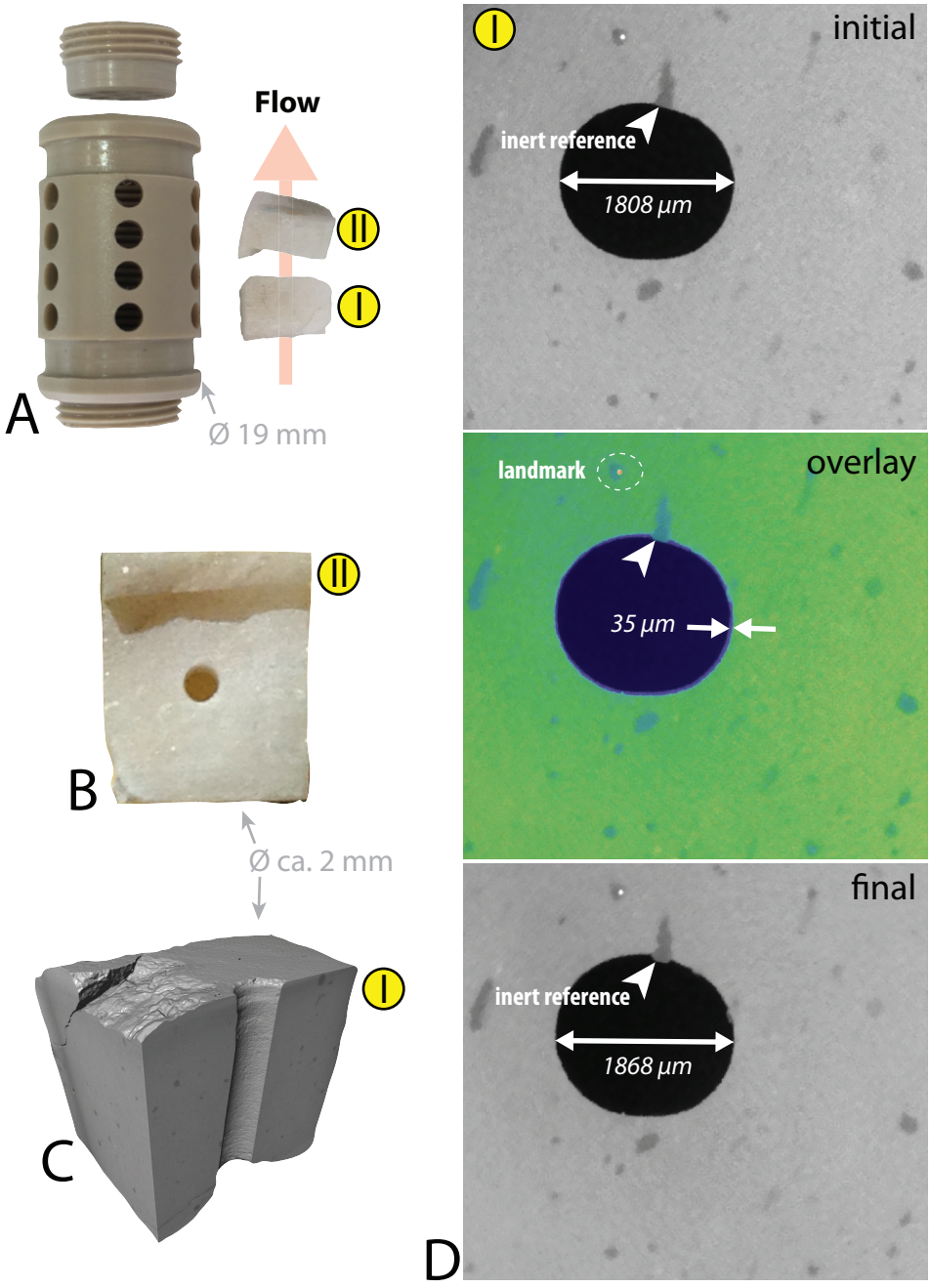

Fig. 2. Visualization of (A) the perforated PEEK chamber for sample assembly in a flow-through experiment with samples (I) and (II), (B) bottom-view of sample (II) and (C) section through volume reconstruction of sample (I). Image sequence of a single reconstructed slice (D) visualizes the surface retreat (overlay) of calcite by comparison of the unreacted (top: initial) vs. reacted (bottom: final) state of the experiment. The view is down the central hole of sample (I), the position of quartz grains as inert reference illustrates the loss of calcite inside the flow channel (center picture: difference). Note the existence of inert, highly attenuating minerals used as landmarks for volume registration.

holder. Both spiderweb-type groove patterns on the end-faces of the standard core holder's inlet and outlet plugs (Kahl and others, 2016), and the perforated lids of the PEEKins enabled direct fluid access to the samples. The marble cuboids were positioned in a stacked order with their central drill holes facing the inlet. Thus, the main flow path runs from the cell inlet through the drill hole of sample I via the drill hole of sample II to the cell outlet. The polycrystalline marble cuboids were reacted using 2.2 mMol Na_2CO_3 solution, equilibrated with air to obtain constant p_{CO2} at pH 9.2, percolating at a flow rate of 0.05 mL/min and 45 bar (4.5 MPa) fluid pressure. Fluids discharged from the cell are passed through a back-pressure regulator that maintains a constant pressure level inside the flow-through apparatus. Since minor fluid transit around the samples (especially around sample II) is possible, the actual flow rate through the drill holes could have been slightly less than 0.05 ml/min.

X-ray μ-CT Surveillance of the Flow-Through Experiment

The X-ray μ-CT scans were performed using the ProCon CT-ALPHA system of the *Petrology of the Ocean Crust* research group at the University of Bremen, Germany. The pierced marble cuboids were scanned before and after the dissolution experiment with a beam energy of 120 kV, an energy flux of 350 μA, and using a thin copper filter in 360° rotation scans conducted with a step size of 0.225°. To achieve a detector resolution of 4.1 μm (sample I) and 3.1 μm (sample II) per voxel, the field of view (FOV) of the μ-CT scans was restricted to the central drill hole of the respective sample. After an acquisition time of 3 hours for each sample, an image volume of 2000 × 2000 × 2000 voxels (or larger) was available. Correction of ring artefacts and reconstruction of the spatial information on the linear attenuation coefficient in the samples was done with the Fraunhofer software VOLEX, using a GPU-hosted modified Feldkamp algorithm based on filtered backprojection (Feldkamp and others, 1984). All subsequent processing of volume data (for example, rendering, filtering of the raw data, segmentation, surface generation *et cetera*) was done using Avizo 9.5 (FEI).

Filtering, Registration and Phase Segmentation of μ-CT Volume Data

In the reconstructed volume data of the impure marble, areas of very high to high attenuation phases (for example, sulfides, calcite; see fig. 2D) are encoded in white or light gray values, whereas areas of low X-ray absorption are color-coded in dark gray (here mica, quartz) or black (voids, cracks). To reduce noise and enhance segmentability, a combination of two digital image filters (anisotropic diffusion with five iterations, and non-local means 2-D) was applied successively to the reconstructed raw data. Thus, the resulting data volume comprises enhanced segmentability due to both preserved edges at the grain boundaries facing the flow channel, and due to smoothing of former noisy areas. On the filtered data sets, a landmark-based registration of both volume reconstructions of initial and final state relative to each other has been performed. Subsequently, an automated 2-D segmentation procedure was employed on the registered data volumes to segment mineral surface from void. The segmented voxels, containing only the solid phases, of both initial and final states of both samples were then selected (binarized) and combined to a 3-D model of the polycrystalline marble samples.

Surface Generation, and Surface Distance Determination of μ-CT Volume Data

To assess the retreat of the reacting flow channel surface during reaction time, the module *Generate Surface* in Avizo 9.5 was employed to create a triangular approximation of the surface of both registered initial and final 3-D models (fig. 3A). Upon surface generation, a modified Gaussian filter was chosen (extend 5 of 9) to smooth the region boundaries of the binarized input 3-D models, which consist of cuboid elements (voxels), that would otherwise produce staircase-like surfaces. We used the module

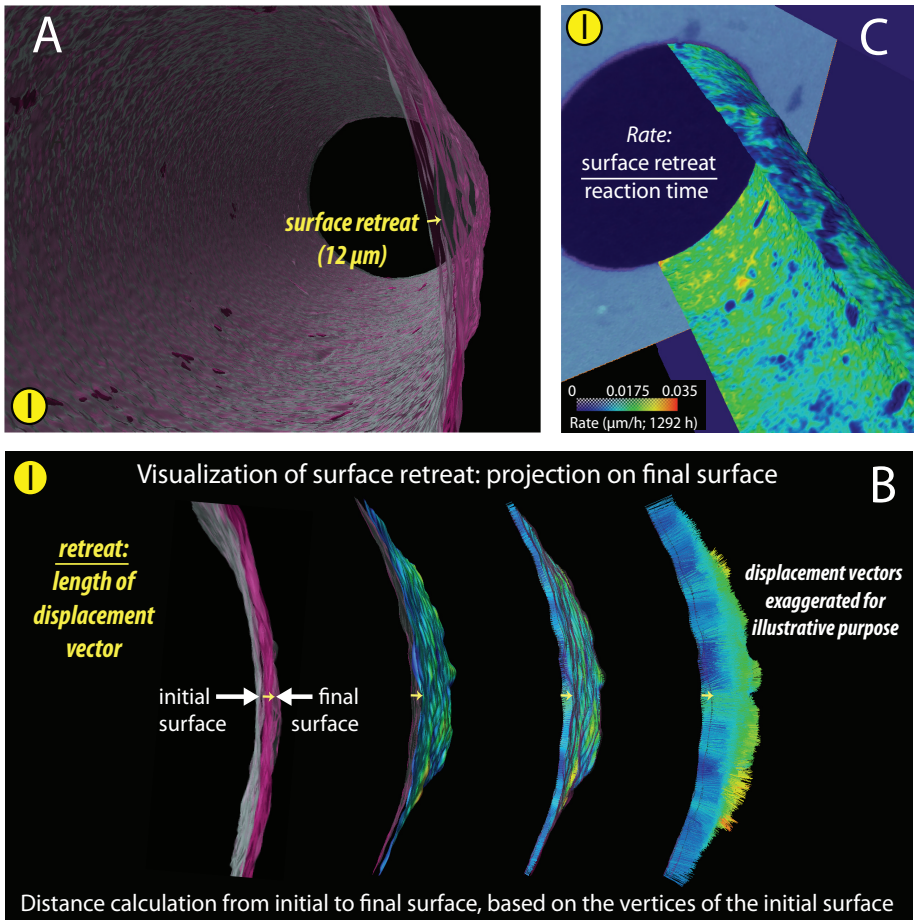

Fig. 3. Determination of surface retreat and rate map calculations from µ-CT volume data (sample I). (A) Triangular approximations of the calcite surface at both initial and final states of the percolation experiment (coloring: initial surface-transparent white, final surface-pink). (B) The displacement information has been projected on the final surface, since it is the final surface that exhibits the contrasting surface retreat of quartz and calcite. For each vertex of the initial, smoothed surface the distance to the closest point on the final, smoothed surface was computed. (C) The conversion of a surface distance map into a rate map (µm/h) is achieved by division of surface retreat by reaction time. (For interpretation of the references to color in this figure, the reader is referred to the web version of this article.)

Surface Distance to calculate the distance between initial and final marble surface models. We chose the final surface to project the displacement information, since it represents the topography of the final reaction state after the experiment. For each vertex of the initial surface, the distance to the closest point on the final surface was computed (fig. 3B). Eventually, the conversion of a surface distance map into a rate map (µm/h, fig. 3C) is achieved by dividing the surface retreat distance by reaction time (Fischer and others, 2012a).

Rate Spectra Extraction from µ-CT Volume Data

The rate distribution of the observed surface retreat has been extracted from the rate map employing the module *Histogram* in Avizo 9.5 with a binning of 0.0002 µm/h.

Several factors may impact the dissolution rates determined by 3-D quantitative image analysis of reconstructed and registered μ-CT scans: the voxel size of reconstruction, the characteristics of the registration method, the method used for segmentation of the mineral phase, the mode of surface generation from the binarized marble model, and the details of the surface distance determination. Even in the current state-of-the-art of CT metrology, the means of finding analytical expressions for the accuracy ('trueness' and precision) of measuring systems with statements of maximum permissible error are still under scrutiny within the scientific community (Villarraga-Gómez and others, 2018). One of the major problems in CT metrology is the difficulty of finding out the correlations between interference effects from the CT measurement process, including data processing steps, and the final CT measurement results (Hiller and Hornberger, 2016). Furthermore, it is still hardly possible to generalize CT results and to transfer results obtained for individual work-pieces to other measuring objects, which (slightly) differ in size and form. This leads in some cases to an underestimation and in some cases to an overestimation of the performance parameters (Moroni and Petrò, 2016; Moroni and Petrò, 2018).

Still, a minimization of potential sources of inaccuracy can be considered. Our strategy to minimize systematic divergences between initial and final 3-D image data is to follow absolutely identical protocols upon creation of the 3-D surface models of the initial and final marble reaction surface. The voxel size of the reconstructed image material is dependent on beam geometry of the scan and camera design. Therefore, all scans designated for later registration should be carried out under identical conditions. For registration of successive scans, different approaches such as point-based (via landmarks) or intensity-based (applicable to volumes of interest) are available. Nevertheless, a successful registration critically depends on the actual attenuation of the investigated sample. If extent and distribution of fabric compounds used for registration are proper, both point-based and intensity-based methods can be applied, even in combination (Li and others, 2006). However, the current marble samples offer only two fabric element contacts with high attenuation contrast, which would be favorable for intensity-based registration: (i) the contact solids-pore space, which is under investigation, and (ii) tiny highly attenuating minerals, currently used as landmarks for volume registration (fig. 2). The extent of the latter is too small to be employed for intensity-based registration methods. Conversely, attenuation contrasts between different marble mineral compounds have been too low to permit proper intensity-based registration. Therefore, registration has been restricted to the landmark-based technique. An automated segmentation procedure has been applied to exclude user-dependent bias on the results. Upon surface generation, the degree of smoothing to generate sub-voxel surface weights to avoid the staircase-like artifacts has been chosen identically, since the number of triangles influence the final surface approximation. The computer hardware provided 130 GB RAM, 24 CPU and a NVIDIA Quattro K6000 graphics card to process the μ-CT image data. In the course of surface distance measures (fig. 3), both samples have been treated the same way to have comparable data.

Rate Maps and Rate Spectra Using Vertical Scanning Interferometry Techniques

A calcite single-crystal sample in optical quality was obtained from Crystal GmbH, Berlin (Germany), and the (10−14) surface was partially masked (Mahan, 2000). The masked surface section served as a reference for height difference calculations after dissolution reactions. Dissolution experiments were performed in a flow-through cell. The fluid volume in the cell was 300 μL. The volumetric flow rate was 30 mL/h. After a pre-reaction period of 90 minutes, we applied three reaction periods of 15 minutes and 60 minutes, respectively. We used a 2.2 mMol Na_2CO_3 solution, equilibrated with air to obtain constant pCO_2 at pH 9.2 for dissolution experiments. Experimental settings

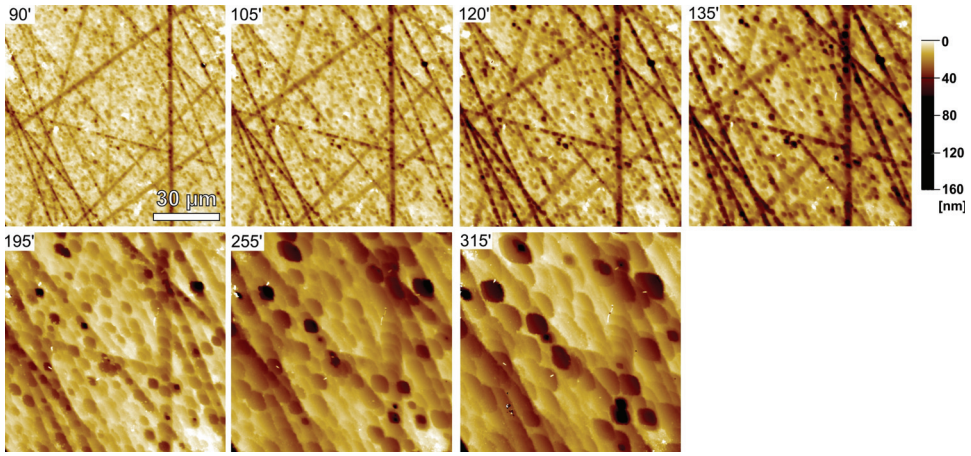

Fig. 4. Calcite single-crystal topography evolution over seven dissolution reaction periods from 90 min. to 315 min. First four data sets were measured using phase shift interferometry; subsequent topographies were measured using white light interferometry technique because the surface height after 135' exceeded the maximum height that can be analyzed using PSI technique. Note the existence of a limited number of "long living", deep etch pits, responsible for elevated materials fluxes at fixed positions over several reaction periods (t = 195–315 min).

similar to those in many calcite dissolution studies in literature were used in order to provide comparable results (Sjoberg, 1978; Chou and others, 1989; Liang and others, 1996; Morse and Arvidson, 2002; Arvidson and others, 2003). For details concerning the experimental setup using polycrystalline calcite and VSI techniques see Bollermann and Fischer (2020), this volume.

Surface Topography Analysis and Calculation of Rate Maps

After each reaction step, the surface topography was analyzed using vertical scanning interferometry (VSI). This method is capable of analyzing sample surface height changes in the range of 0.1 nm using phase shift interferometry (PSI) or 1 nm using white light interferometry (WLI) techniques. We applied a ZeMapper interferometer system (manufacturer: Zemetrics, Tucson, AZ) equipped with five interferometry objectives (Fischer and others, 2012b). The more sensitive PSI mode was utilized for the three initial and short reaction periods (each 15'). Reacted surfaces after three subsequent reaction periods (each 1 hour) were measured using the WLI measurement mode (fig. 4).

Using the inert surface section as a height reference, six height difference maps were calculated after each reaction step. The height difference (dz) per reaction time (dt) of each (x,y) map point contains information about the height retreat velocity (dz/dt). The material flux map was used to calculate the rate map by dividing each (dz/dt) value by the molar volume $V_m = 36.9\ cm^3/mol$.

Reactive Transport Modeling

We employ a mathematical approach for modeling the coupled processes of fluid flow and calcite dissolution in the connected free-flow region. In the mathematical model, we employ the Stokes-Brinkman equation for momentum balance, which is a unified equation for modeling fluid flow in the entire domain. We then couple the Stokes-Brinkman equation and the reactive-transport equations for simulating the coupled processes.

The Stokes-Brinkman model.—The Stokes-Brinkman equation has been widely applied to model fluid flow in fractured porous media (Bi and others, 2009; Popov and others, 2009; Qin and others, 2010; Yuan and others, 2016; Yuan and others, 2019b), as it provides a single set of equations for simulating fluid flow in the entire domain. The general formulations of the Stokes-Brinkman equation for incompressible single-phase fluid are given as follows (Brinkmann, 1947; Bi and others, 2009; Popov and others, 2009; Qin and others, 2010; Yuan and others, 2016):

$$\mu \mathbf{K}_{\mathbf{perm}}^{-1} \mathbf{v} + \nabla p - \mu^{*} \Delta \mathrm{v} = 0, \tag{1}$$

$$\nabla \cdot \mathbf{v} = 0, \tag{2}$$

where **v** represents the physical velocity of the fluid in free-flow regions and the Darcy velocity in porous media, p denotes pressure, $\mathbf{K}_{\mathbf{perm}}$ is a permeability tensor, μ is the physical viscosity of the fluid, and μ^* is the effective viscosity. The effective viscosity μ^* is a key parameter for matching the shear stress boundary condition at the interface between free-flow and porous media (Martys and others, 1994). The effective viscosity μ^* is set equal to the fluid viscosity, $\mu^* = \mu$ in most applications (Bi and others, 2009; Popov and others, 2009; Qin and others, 2010; Yuan and others, 2016; Yuan and others, 2017; Yuan and others, 2019b). In this paper, $\mathbf{K}_{\mathbf{perm}}$ is set as a very large number in the free-flow region. Eq. (1) can be reduced to the Stokes equation. The readers are referred to (Yuan and others, 2016) for more details on discussions of the Stokes-Brinkman equation.

The reactive transport model.—The reactive transport equations describe the coupled processes of solute transport and geochemical reactions. In the model, the aqueous species are classified into primary species and secondary species (Steefel and Lasaga, 1994). The general mass conservation equations integrating flow, solute transport, and chemical reactions for the primary species α are written as:

$$\frac{\partial C_{T\alpha}}{\partial t} + \nabla \cdot (v C_{T\alpha} - D \nabla C_{T\alpha}) = R_{\alpha}^{min}, \ (\alpha = 1, \ldots, N_p). \tag{3}$$

In equation (3), N_p is the number of primary species. $C_{T\alpha}$ are the total concentrations of primary species. $R_{\alpha}^{\min}$ are the kinetic reaction rates of primary species α, which are calculated by:

$$R_{\alpha}^{\min} = \operatorname{sgn}(\log \Omega) A k (\Pi_{i=1}^{N} \alpha_i^{\lambda}) |1 - \Omega|,$$

where k is the rate constant, Ω is the saturation state, and A is the reactive surface area of the calcite (in unit of m^2 per m^3 mineral rock). The reactive surface area, A, is expressed as $A = A_{ssa} \rho \phi_m$, where ϕ_m is the volume fraction of mineral, A_{ssa} is the specific surface area (in unit of m^2/g), and ρ is the mineral density.

In this paper, the coupled mathematical model is solved numerically in a sequential fashion. The readers are referred to Yuan and others (2019b) for more details on the numerical discretization and solutions for the Stokes-Brinkman equation and reactive transport equations. Note that the numerical scheme can be embedded in a nonlinear iteration until the desired accuracy is reached. For simplicity, we do not use such nonlinear iterations in our current study.

RESULTS AND DISCUSSION

We compare the spatiotemporal reaction rate heterogeneity of two dissolving types of calcite. Polycrystalline calcite dissolution reactions are performed for up to 54 days while single-crystal calcite surfaces are reacted for up to 315 minutes.

Calcite Dissolution on the Grain Scale and Above: μ-CT-Derived Rate Maps

Surface reactivity of polycrystalline calcite aggregates in the μ-CT flow-through experiment was assessed by quantification of the surface retreat during reaction time. Two mm-sized marble cuboids (fig. 2) samples were stacked in a perforated reaction chamber and scanned before and after reactive fluid was percolated for 1292 h. Unlike VSI, the determination of surface retreat by μ-CT surveillance is not restricted to a vertical geometry. In principle (using the module Surface Distance in Avizo 9.5, see method section), determination and visualization of the surface retreat during reaction time can be approached from two perspectives: (i) computation from initial to final surface, based on the vertices of the initial surface, and (ii) surface distance calculation from the final to the initial surface, based on the vertices of the final state. Potential differences are caused by distinctions between the initial and final marble surfaces (pre- and post-experiment) which involves slightly asymmetric assessment by the vertex-based surface distance measures (see supplementary fig. A1). Here, we chose (i) and the projection of the results onto the final surface (fig. 3B). Since the determination of surface retreat is based on two surface models with smoothed region boundaries (no staircase-like voxel surfaces are involved), the surface distance calculation delivers values within in the sub-voxel range.

The volumes of interest (VOI) chosen for detailed inspection of dissolution rates (fig. 5) cover a height of 4.1 mm (sample I) and 3.7 mm (sample II), respectively. The color-coded 3-D rate map (fig. 5) shows site-specific dissolution rates of calcite on the microscale, projected on the final surface (fig. 3C). Exposed quartz and mica grains are characterized by negligible material loss. Although the dissolution rates have been determined for the entire surface of the drill holes, rate spectra analyses for both samples were restricted to regions of interest (ROI). ROI (see semitransparent whitish areas in fig. 5) have been chosen to avoid mica- and quartz-rich regions, which show considerably lower dissolution rates than calcite. Representative ROIs of both samples are depicted in figure 6 alongside with sections through the volume reconstructions to show the similar density of quartz and mica grains on the surface of the central drill hole within the impure marble specimen.

The residence time of the fluid defines the existence of transport- vs. surface-controlled reaction conditions. Liang and Baer (1997) showed the transition from transport-controlled to surface-controlled conditions at about 50 to 100 μL/min. By applying a flow rate of 50 μL/min, we anticipated surface-controlled conditions close to the inlet of the reacting flow in sample (I) and increasing impact of flow control towards the flow outlet (sample (I)), because of an increase in ion concentration. Sample (II) is in serial connection to sample (I), thus the fluid shows elevated ion concentration already when entering sample (II). In this case, the reaction conditions for sample (II) are always transport-controlled. Both rate map and rate spectra results confirm this assumption (figs. 5–7). Sample (I) shows the anticipated rate gradient from high to low reactivity while sample (II) continues the low reactivity due to transport-controlled conditions, similar to the outlet section of sample (I). A gradient towards overall lower rates is visible in the set of spectra curves of sample (I), indicating a concentration shift to more close-to-equilibrium conditions (fig. 7). Figure 8 visualizes this gradient in the rate map that includes the inlet section of the sample with the highest surface rates. While the rate gradient owing to transport conditions is clearly shown, the superimposition of surface reactivity is equally important to the rate results. Regardless of the impact of saturation, the overall rate range of about two orders of magnitude is ubiquitous.

Additional information in figure 7 provides comparison to surface-controlled rate data based on interferometry techniques (upper section). The overall rate range is 10^{-9} to 2×10^{-7} mol m^{-2} s^{-1}. This dataset includes initial surface rates, collected

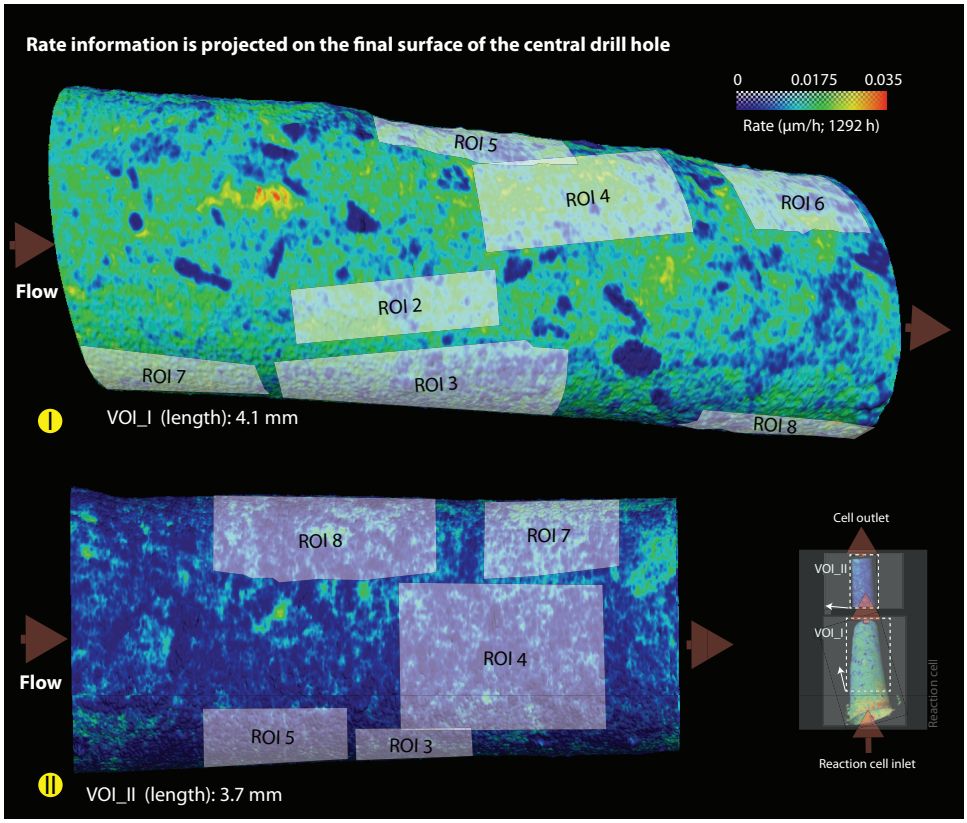

Fig. 5. 3-D maps of calcite dissolution rates on the surface of central drill holes in samples (I) and (II). The color coding illustrates both mineral- and site-specific dissolution rates over 54 days of percolation. In general, the rate range observed for sample (I) is larger than for sample (II), depicting the effect of assembly and relative positioning with respect to the fluid passage within the sample containment. The volumes of interest (VOI) containing the walls of the central drill hole cover a length of 4.1 mm (sample I) and 3.7 mm (sample II), respectively. Exposed quartz and mica grains are characterized by negligible material loss. Semitransparent whitish areas refer to regions of interest (ROIs) evaluated for rate spectra analysis. ROIs were carefully chosen to exclude mica- or quartz-rich regions.

during reaction periods of 15 minutes (green curves, PSI measurements). This data set is homogeneous. Almost no dispersion of higher rate portions at about 10^{-7} mol m^{-2} s^{-1} is found. This picture changes during ongoing reaction time and reaction periods of 1 hour (blue curves, WLI measurements) and shows a dispersion of rate portions. Here, the occurrence of lower rate portions is rather homogeneous. Higher rate portions at about 10^{-7} mol m^{-2} s^{-1} show higher variability, especially when compared to data collected with larger field-of-view (dark-blue curve). This result indicates a spatial heterogeneity with respect to surface reactivity and rate distribution. For comparison, we show literature data of a long-term dissolution experiment that has been analyzed by using a FOV of ~130,000 μm^2, that is, 16 times greater than the FOV of the interferometry data presented here. After the reported reaction period of 4.5 hours, a minor section of the reacting surface is characterized by remarkably high surface rates due to fast-moving surface steps (Bibi and others, 2018). Thus, the temporal and spatial heterogeneity of surface rates requires a sufficiently large FOV to be captured. Additional data (WLI, calcite marble) illustrate the rate spectrum

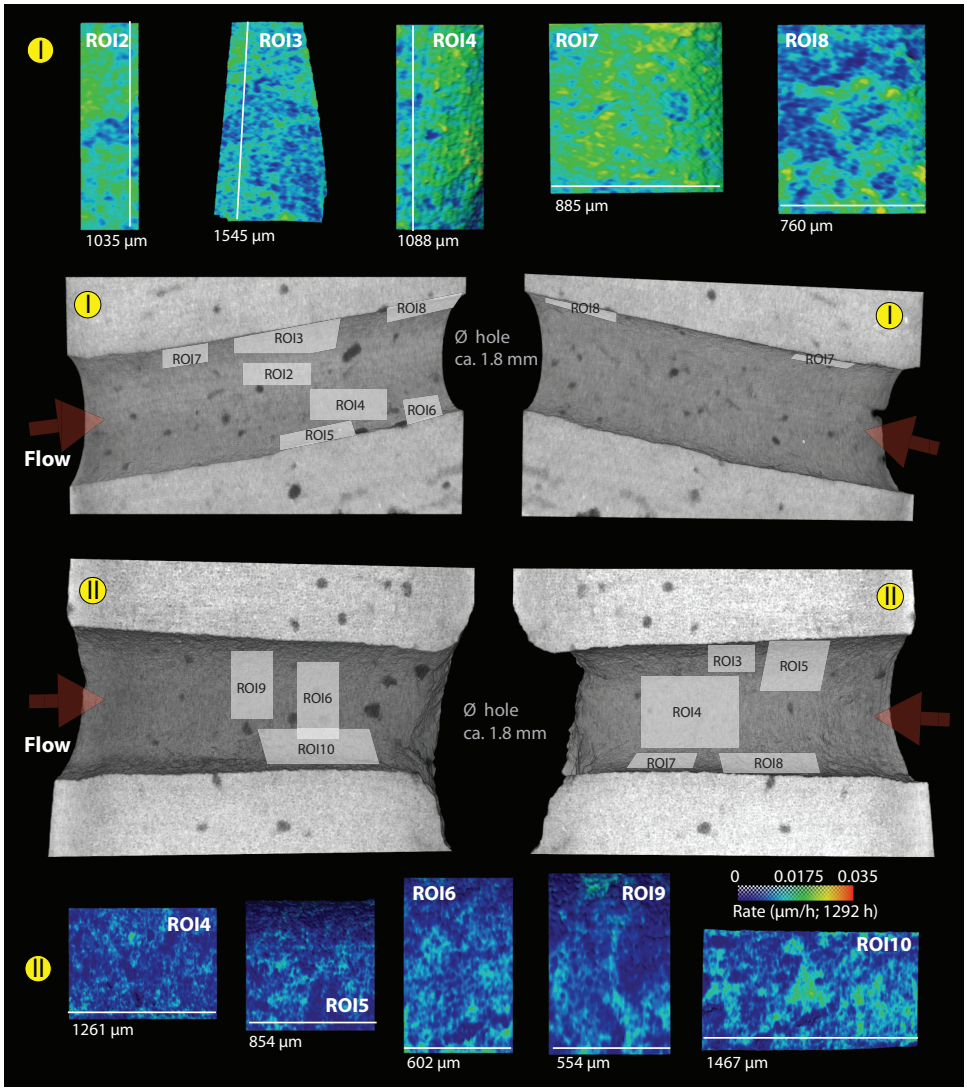

Fig. 6. Representative regions of interest (ROI) of samples (I) and (II) displaying the varied dissolution during the percolation experiment. Sections through the volume reconstructions show the similar density of quartz and mica grains within the impure marble specimen.

measured on dissolving polycrystalline calcite using white light interferometry. The rate data include higher rate portions ($> 10^{-7}$ mol m^{-2} s^{-1}) compared to single-crystal dissolution experiments analyzing relatively small field-of-view sections of *ca.* 100 µm × 100 µm. Higher rates of large surface steps are reported from an even bigger field-of-view of about 400 µm × 300 µm (Bibi and others, 2018). The here reported VSI rate data illustrate the general similarity of rate spectra of polycrystalline and single-crystal calcite. Differences in crystal orientation do not result in measureable differences of observed rate ranges of single-crystal vs. polycrystalline materials, similar to previous results (Smith and others, 2013a). Observed differences are attributed to the impact of accumulated defects at grain boundaries as well as the evolution of high

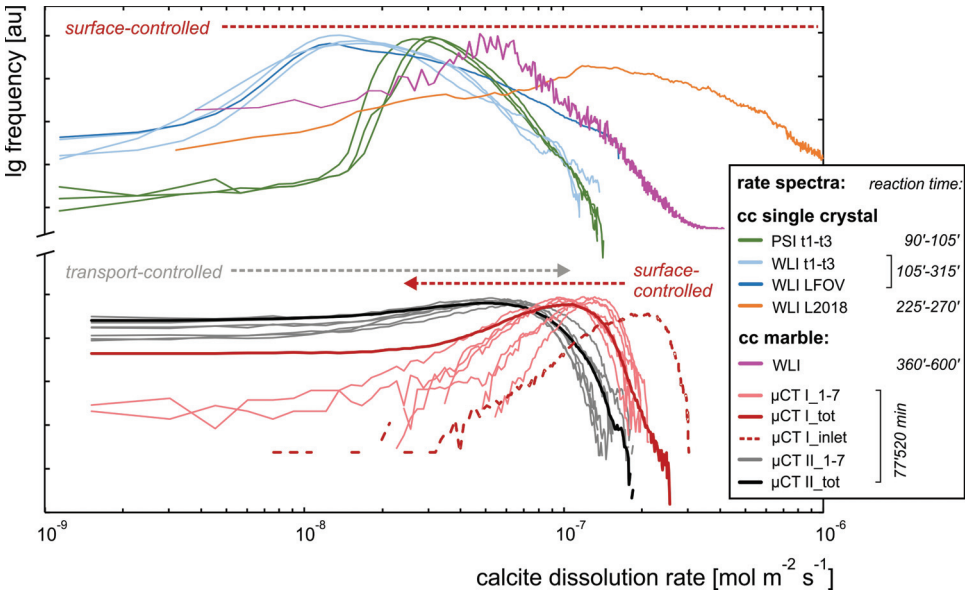

Fig. 7. Compilation of calcite single-crystal and polycrystalline calcite dissolution rate spectra data. Lower section: Calcite marble dissolution rate spectra based on µ-CT measurement capabilities include the two samples I and II. Total rate spectra (I_tot, II_tot) and spectra of data subsets (I_1-7; II_1-7; compare fig. 5) are shown. Spectrum I_inlet shows the solely surface-controlled µ-CT rate portions vs. mixed surface- and flow-controlled rate data I/II_1-7, compare figure 8. Upper section: Rate spectra of dissolving single-crystal and calcite marble (WLI) based on interferometry techniques include white light interferometry data with large field of view of 300 µm × 300 µm (WLI_LFOV), a temporal sequence of white light interferometry data (WLI_t1-t3: 135 min – 195 min – 255 min – 305 min) as well as a temporal sequence of phase shift interferometry data (PSI_t1-t3: 90 min – 105 min – 120 min – 135 min) and additionally white light interferometry data from literature (WLI_L2018: Bibi and others, 2018). Frequency of rate components is given in logarithmic scale, arbitrary units.

kink site densities along large surface steps that developed during coalescence of etch pits (Luttge and others, 2007; Luttge and others, 2013; Fischer and others, 2014; Luttge and others, 2013; Fischer and others, 2014; Kurganskaya and Luttge, 2016; Fischer and Luttge, 2017). More details of this dataset and interpretations about rate heterogeneity are discussed in Bollermann and Fischer, 2020.

At the same time, a sufficiently large spatial resolution is required in order to analyze properly the material flux. Thus, an overlap of FOV and spatial resolution of both methods, µ-CT and interferometry, is required to provide quantitative insight into the heterogeneity of surface rates. More specifically, standard interferometry FOV sizes might be too small to include rare high-reactivity surface steps and the highest spatial resolution of µ-CT measurements might be insufficient to map small but reactive surface portions. While the combination of both methods provides a unique opportunity to bridge surface rate data from the micron to millimeters scale the data need a careful evaluation because of the changing spatial resolution and FOV size. Both parameters act like a band-pass filter system thus potentially eliminating sections of the highest and lowest rate portions.

Comparison of Rate Distribution Data to Reactive Transport Modeling Results

We investigate numerically the fluid flow through a simple cylindrical channel without any surface roughness and analyze the transport-controlled surface reactivity. The diameter of the flow channel is 1.8 mm, see figure 8. The fluid with pH = 9.2 is

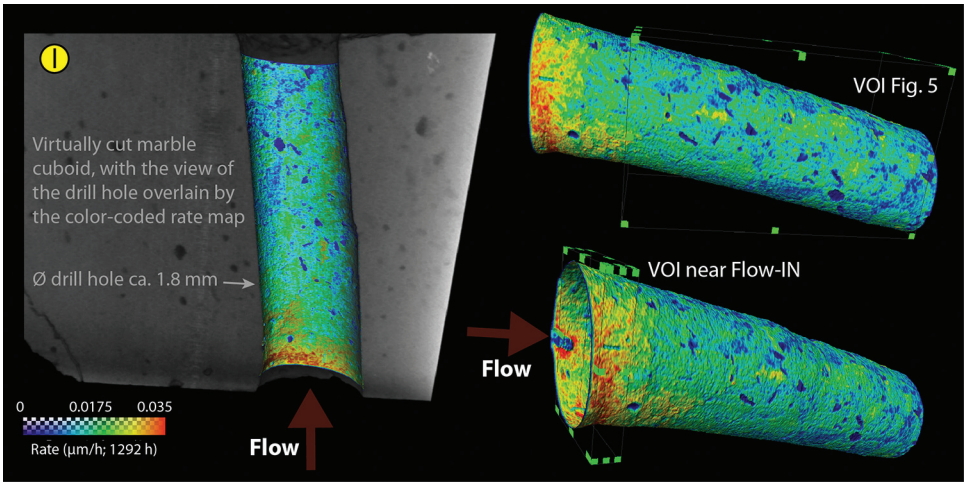

Fig. 8. Visualization of the gradient in the µ-CT-derived reaction rates observed on the calcite surface of the central drill hole in sample (I) in a 54 days flow-through experiment. The inlet section of the sample exhibits the highest surface rates, being located towards the fluid inlet of the percolation cell. The profile indicates surface-controlled conditions close to the inlet of the reacting flow and increasing impact of flow control towards the flow outlet. The length of FOV is 5.7 mm. While on the left the rate map can be seen from inside flow channel, on the right it is depicted from the outside (see fig. 3).

injected into the cylindrical borehole at a constant injection rate of 0.05 mL/min. Since this linear flooding case study has a symmetric geometry and symmetric boundary conditions, the three-dimensional problem is simplified to a two-dimensional problem with a significant decrease in computational time.

Based on the mass balance, the normalized dissolution rate at the channel surface is calculated as (Li and others, 2008; Luquot and Gouze, 2009):

$$R_n = \frac{(C_{Ca|out} - C_{Ca|in})\, Q_{inj}}{A_{tot}},$$

where $C_{Ca|in}$ is the concentration of calcium ions at the inlet, $C_{Ca|out}$ is the concentration of calcium ions at the outlet, Q_{inj} is the injection rate, and A_{tot} is the total surface area. (Li and others, 2008) presented a simple definition of A_{tot} considering the geometry of the pore, which could underestimate the surface area without considering surface roughness. Here, we utilize the surface roughness factor (RF) combined with the geometric surface area (Thomas, 1999) to implement the effect of rough mineral surfaces. The modified surface area, A_{tot}, is expressed as $A_{tot} = (2\pi rL)F$. However, the reader is referred to the discussion highlighting the fundamental problems of surface area normalization of reaction rates (Fischer and others, 2012a).

Nonetheless, we illustrate three case studies using the current reactive transport approach. The parameters are given in table 1.

The parametrization of surface reactivity is underdetermined since both, surface area and reaction rate "constant" are varying in such systems, as discussed by, for example, Arvidson and others (2003). *Case 1* utilizes data by Busenberg and Plummer (1986). Comparatively high surface area and rate are due to small grain sizes ("synthetic rhombohedrons, analytical reagents"). *Case 2* exemplifies the simple reduction of the rate due to the decrease of surface area. In *case 3*, $logR_n$ is -6.25 mol m^{-2} s^{-1}, which is higher than the VSI-derived dissolution rate by Arvidson and others (2003). Using *case 3* as a starting point, the modification of the surface roughness factor results

TABLE 1

Parameters used for three cases of reactive transport modeling, applying contrasting values of specific surface area and normalized mean rate

Case	A_{ssa} [m^2/g]	log Rn [mol m^{-2} s^{-1}]
# 1	0.19[1]	-5.8[1]
# 2	0.019[2]	-6.8
# 3	0.19	-6.25[3]

In all cases the roughness factor is set = 1. The parameters refer in part to literature data: (1) Busenberg and Plummer 1986; (2) the specific surface area is estimated for the material in this study based on the assumption of powder vs. bulk samples; (3) the mean dissolution rate is modified in order to describe experimental mean rate data.

in reduced $logR_n$, as shown in table 2. This simple calculation exemplifies the current limitations of the reactivity part of reactive transport simulation approaches. Instead, reaction rate data using μ-CT and VSI techniques do not rely on any surface area normalization, thus quantifying a snapshot of the critical *range* of surface reactivity. RTM approaches are dealing with a *single* rate only and a single surface area value, that is, specific surface area or geometric surface area and a surface roughness factor et cetera, for normalization. To fulfill the simple constraint of a constant mean rate at given chemical conditions the model would require lowered reaction rates for enhanced surface roughness factors (table 2).

Current pore-scale RTM approaches explain any decrease in reaction rates via transport-controlled conditions. Locally enhanced reaction rates cannot be explained by using a simple mean reaction rate.

Figure 9 illustrates this simple situation. Figure 9A shows a cross-section through the fluid velocity distribution. A boundary condition is the constant velocity at the inlet (velocity of each grid block is constant along the vertical axis at inlet). Thus, a certain length parallel to the flow direction is required for developing the *Stokes flow* situation, resulting in the calculated velocity distribution based on the momentum balance. Under steady-state flow conditions (fig. 9A) a static fluid chemistry is observed for both, Ca^{2+} ion concentration distribution (fig. 9B) and pH distribution (fig. 9C).

This provides quantitative insight into the axial decrease in reactivity due to fluid flow and residence time and explains the rate gradient observed in figure 8. We utilize this information and compare experimental and simulation results in figure 10.

TABLE 2

Effect of increased roughness factor F on resulting mean calcite dissolution rates Rn.

F [-]	log *Rn* [mol m^{-2} s^{-1}]
1	-6.25
5	-6.95
10	-7.25
20	-7.55
30	-7.73

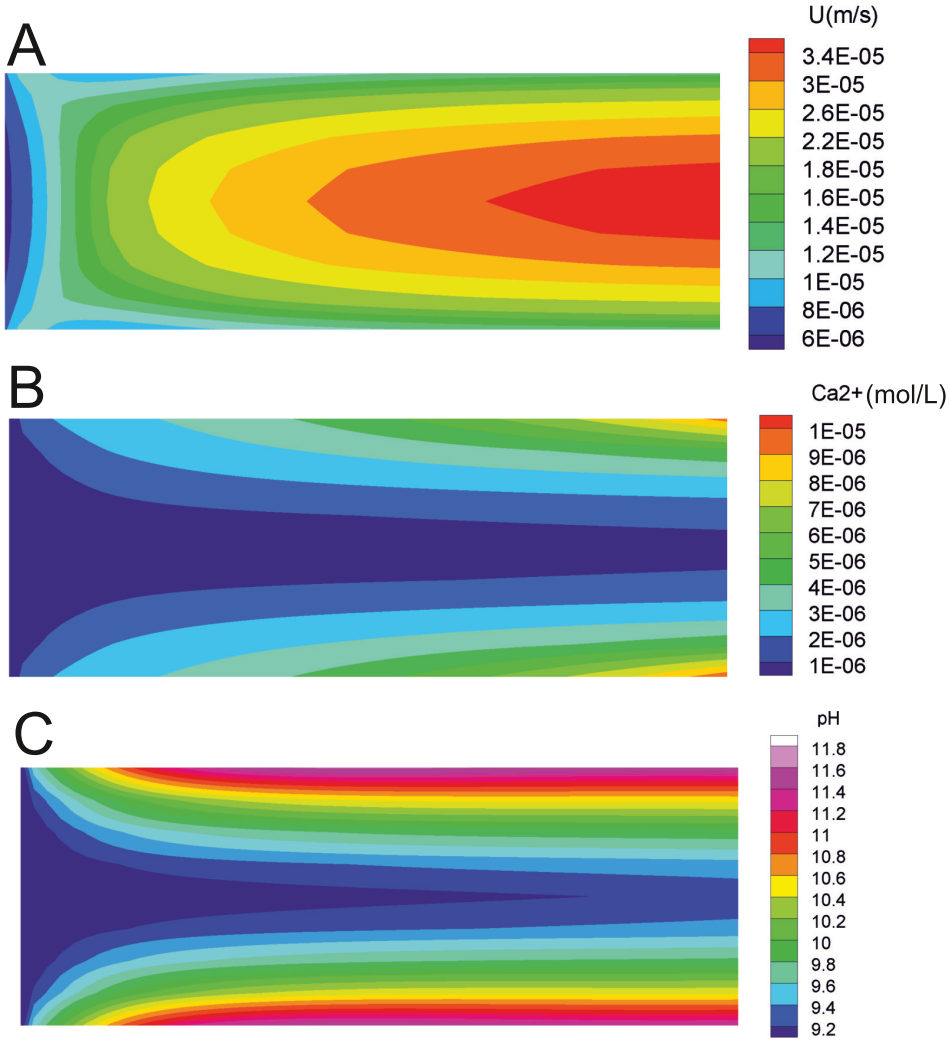

Fig. 9. Reactive transport simulation results, describing the steady-state fluid flow through the cylindrical channel (L = 5.5 mm) as a 2-D situation. Velocity (A), Ca^{2+} concentration [mol/L] (B), and pH (C) maps illustrate the static gradient from inlet (left) to outlet (right).

A recent study follows a similar approach, in order to analyze the local variability of dissolution rates of multiple calcite crystals distributed in a flow-through column (Bouissonnié and others, 2018). The authors show in this thorough study the decrease of dissolution rates as a function of column length and, thus, saturation. While they do not highlight the local rate variability of each sample, they were able to explain successfully the results by applying the stepwave model (Lasaga and Luttge, 2001) while the results are at odds with an explanation derived from transition state theory (TST).

Figure 10 provides detailed insight into the current limitation of reactive transport modeling approaches. The primary issue is the parametrization of surface area and rate constant in order to quantify surface reactivity with a constant value. While this parametrization (*case 3*) is able to simulate the observed mean dissolution rate close to the outlet it fails to describe the mean rates observed at the inlet. Instead, this

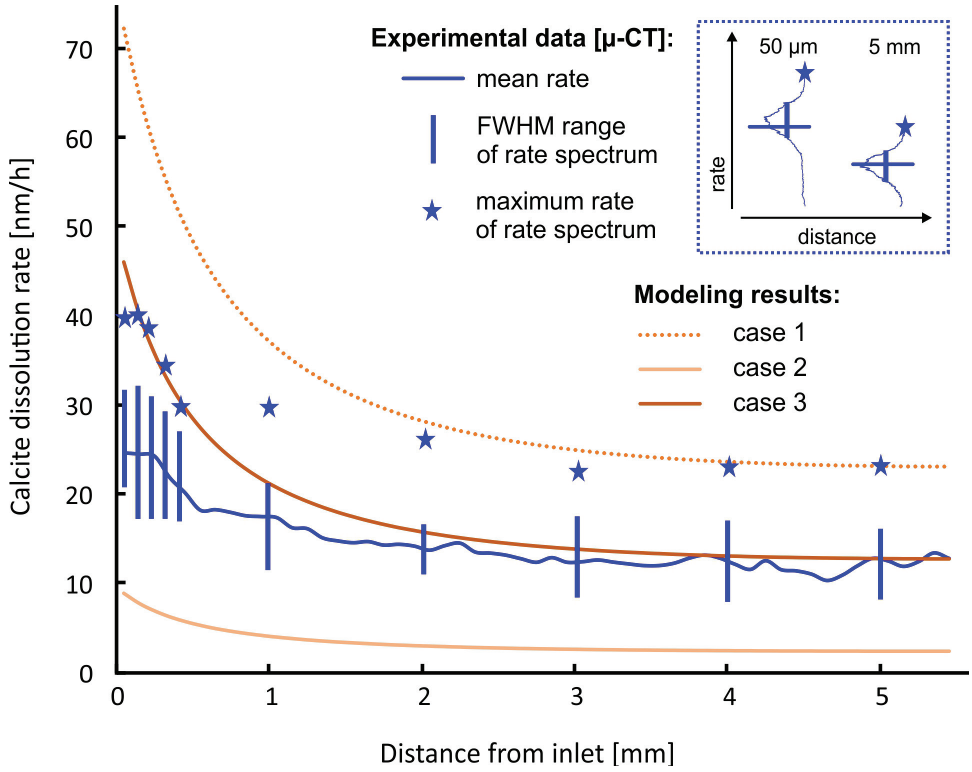

Fig. 10. Comparison of measured dissolution rate data with results of reactive transport modeling using three parameter combinations (case 1–3) of surface area and reaction rate "constants", see table 1. Note the observed discrepancy of modeled mean rates: While the parameter combination of case *3* describes the observed maximum rates in the experiment close to the inlet, the parameter combination of case 1 simulates the maximum rates close to the outlet.

parameter combination resembles the experimental maximum rates, which are about two times higher than the problematic mean values of partly non-GAUSSian rate distributions (fig. 11). Inversely, a parametrization of the reactivity simulation in order to fulfill the maximum rates observed at the outlet (*case 1*) results in elevated rates close to the inlet that are much higher than any measured dissolution rate portions.

Figure 11 shows examples of several rate spectra analyzed from rate map portions along the reacting surface. Each spectrum integrates over a cylindrical sample section, that is, a ring-shaped map with a width of 100 µ*m* (fig. 11A). Even though each rate map section and the related spectrum average 45,000 or more of single rate data, the resulting rate distributions differ significantly in shape and rate range. As an example, multimodal rate distributions are observed (fig. 11B) that are not adequately described using a mean rate.

The modeled mean rate values (fig. 11B, hexagons, parameter *case 3*) are compared to the measured rate distributions and illustrate the above-mentioned problem. The current way of parameterization of surface reactivity may be able to describe the surface reactivity partly (see, for example, $l = 3150–5250$ µ*m*, fig. 11B). The predicted rates close to the inlet ($l = 50–450$ µ*m*) are, however, far from any experimentally observed mean or maximum rate.

The non-GAUSSIAN rate distribution of reacting materials – independently of transport- or surface-controlled conditions – requires a new strategy of reactive transport modeling. High vs. low reaction rate portions exist even after long reaction

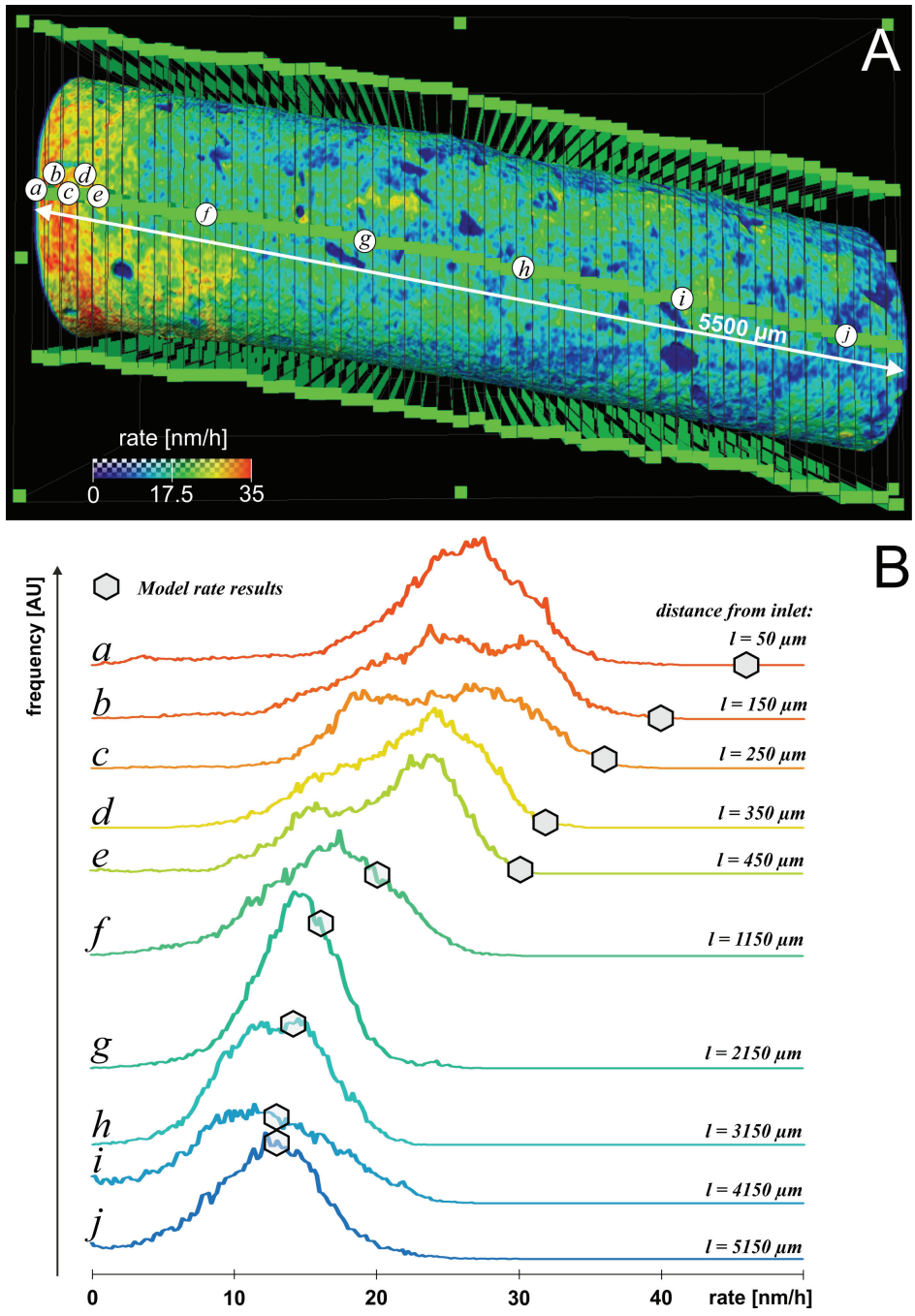

Fig. 11. Rate spectra illustrate the competing impact of transport and material surface properties. Ring-shaped rate map sections (A) are the basis for calculating rate component frequency distributions (B). Modeled mean rates (hexagons, case 3, fig. 10) are compared to each specific rate spectrum.

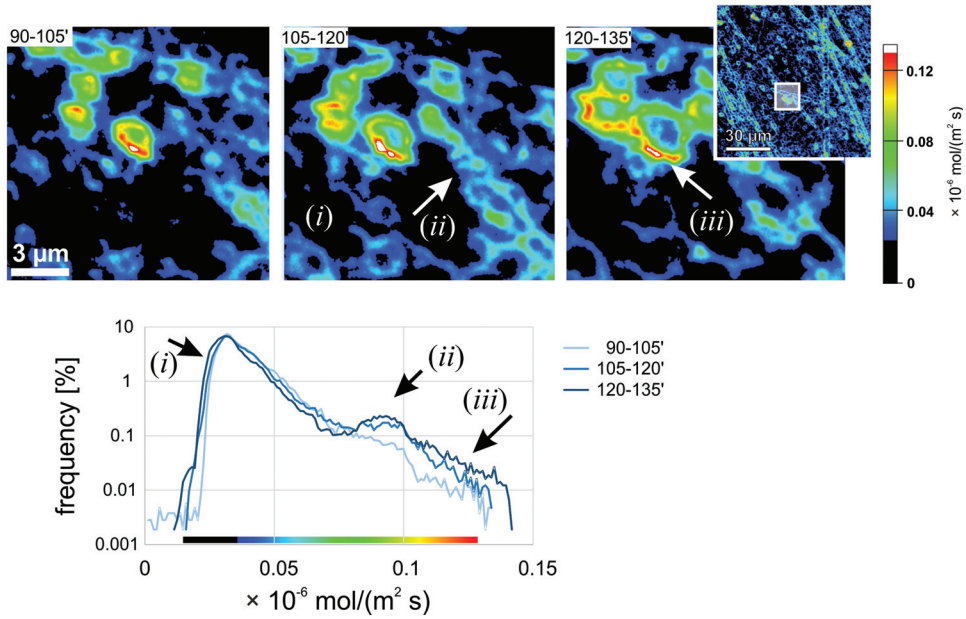

Fig. 12. Rate map and spectra details visualizing the temporal variability of higher rate components (0.07–0.14 × 10−6 mol m^{-2} s^{-1}). The data shown here focus on subsets of the rate spectra presented in figure 7, PSI data, t1-t3, in order to compare the temporal stability vs. dynamics of rate components.

periods. Thus, we suggest taking advantage of the observations of multiple rate modes. Current reactive transport approaches use a single rate constant as a function of extrinsic parameters (for example, pH, electrolyte concentration, T, *et cetera*) for describing the reactivity term. The above discussion and the comparison of measured vs. calculated rate data illustrate the unsatisfactory application of a single rate constant, see figure 10. Here, two rate "constants" (case 1 and case 3) describe at the same time important aspects of the observed rate range. This observation challenges again the continuum description of porous media reactivity and related assumptions required for reactive transport modeling, as previously discussed in detail by Noiriel and Daval (2017).

We did not observe any locally elevated material flux owing to grain detachment from the reacting surface, as described by Emmanuel and Levenson (Emmanuel and Levenson, 2014). Such behavior is unlikely for this material because the crystal size in the sample investigated here is one to two orders of magnitude bigger. Briefly, the next paragraph highlights the rate modes that contribute to elevated rate portions and their temporal evolution.

We analyzed the highest rate contributions calculated from PSI data in a time-sequence of rate maps and spectra (fig. 12). The data suggest uniformly low rate contributions but a rather variable frequency distribution and evolution of high rate portions. The increase of highly reactive surface portions over reaction time underscores the above discussion about the local accumulation of high surface rates, a result this is also related to the temporal dynamics of recently reported so-called pulsating rate contributions (Fischer and Luttge, 2018). In contrast, the lower rate portions ($< 0.07 \times 10^{-6}$ mol m^{-2} s^{-1}) show a rather constant frequency distribution. This is because of the relatively low frequency of high rate contributors, compared to the much higher frequency of low rate portions. It seems to be contradicting that the rate

contributions from highly reactive surface sections are however able to form stable rate contributors, as reported from long-term experiments (Bibi and others, 2018). An explanation is again the length-scale dependency of such observations. Large field-of-view (> 100 μm image length) observations using low-magnification VSI techniques are required to identify such behavior and accumulation of high kink site density features (Bollermann and Fischer, 2020), thus providing an observational link to rate analysis using μ-CT.

SUMMARY AND CONCLUSIONS

In this study, we quantify the dissolution rate variability covering the nm- to mm-scale of dissolving single-crystal and polycrystalline calcite samples, using a combined approach of X-ray micro-computed tomography (μ-CT) and vertical scanning interferometry (VSI). By utilization of μ-CT-derived surface models (ascertained to both initial and final reaction state) for rate determinations analogous to the VSI technique, we analyzed the spatiotemporal heterogeneity of surface reaction rates using the rate map and rate spectra concept. For our percolative μ-CT experiment, we chose a simple, yet effective flow path geometry to avoid strong heterogeneities of the flow field invoked by complex pore networks that can significantly decrease tortuosity and increase hydraulic radius within the reaction time of an ongoing experiment (Flukiger and Bernard, 2009; Noiriel and others, 2009; Pereira Nunes and others, 2016b). Our μ-CT sample setup provided varied fluid flow conditions for two equivalent samples reacted in the same percolation experiment, and yet maintains constant local advective conditions and flow path geometry (the cylindrical pore of a drill hole) over the full reaction time.

Along the entire flow path we observed a heterogeneous surface reactivity which is responsible for heterogeneous, site-specific dissolution rates (spot size: 50–250 μm), indicating the minor impact of crystal orientation vs. local accumulation of highly reactive surface sites, that is, the kink site density. In addition, we detect a general gradient in surface rates which is explained by transport-controlled conditions, as confirmed by reactive transport modelling. Correspondingly, the spatially heterogeneous rate distribution on the grain scale is superimposed to the large-scale gradient.

Using a combined approach of X-ray micro-computed tomography (μ-CT) and vertical scanning interferometry (VSI), we were able to extend the field of view to roughly $5700 \times 9400\ \mu m^2$. The μ-CT data underscore the concurrent and superimposing impact of surface- vs. fluid flow-controlled rate portions. We suggest utilizing the quantification of the combination of both controlling parameters for reactive transport simulation concepts. The new experimental data allow for a quantitative parametrization of reactive transport models at the grain or pore scale and above.

ACKNOWLEDGMENTS

We thank Siegfried Siegesmund (Georg-August-Universität Göttingen) for marble sample material. We thank R.S. Arvidson for helpful discussions and M. K. B. Mahbub and E. T. Pedrosa for assistance in the lab. W.A.K. and W.B. are grateful for funding by DFG Reinhart Koselleck Project [grant no. BA 1605/10-1], CF gratefully acknowledges financial support by the German Research Foundation, DFG grant FI 1212/7-1 as well as by the BMBF, grant 02NUK053B and the Helmholtz Association (Grant SO-093). We acknowledge the constructive reviews by Damien Daval, Bastien Wild, and an anonymous reviewer, as well as the careful editorial work of Rolf S. Arvidson in handling this manuscript.

APPENDIX

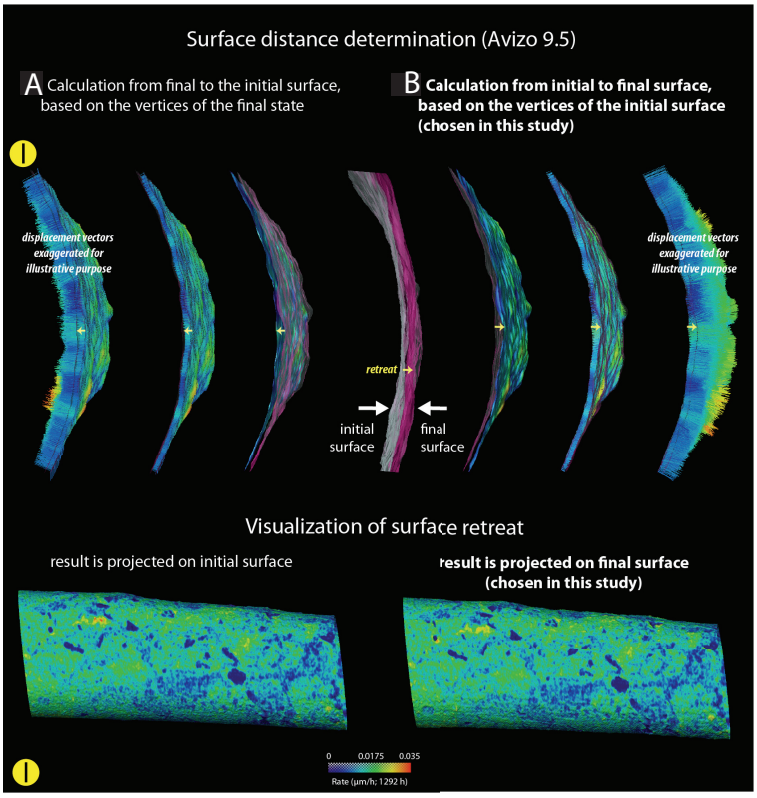

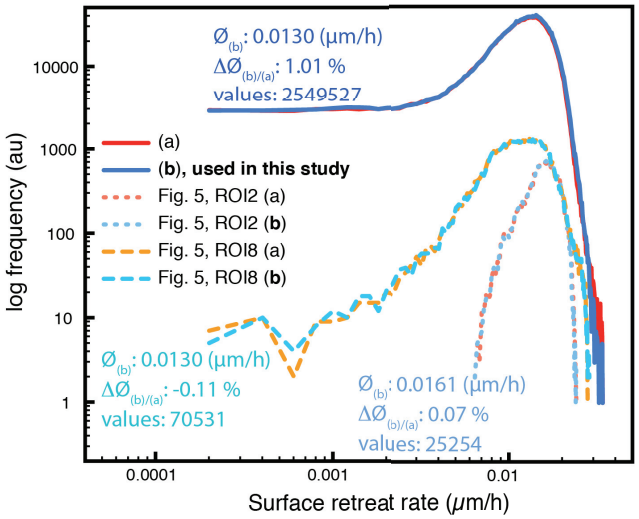

Fig. A1

REFERENCES

Arvidson, R. S., Ertan, I. E., Amonette, J. E., and Luttge, A., 2003, Variation in Calcite Dissolution Rates: A Fundamental Problem?: Geochimica et Cosmochimica Acta, v. 67, n. 9, p. 1623–1634, https://doi.org/10.1016/S0016-7037(02)01177-8

Bera, B., Mitra, S. K., and Vick, D., 2011, Understanding the micro structure of Berea Sandstone by the simultaneous use of micro-computed tomography (micro-CT) and focused ion beam-scanning electron microscopy (FIB-SEM): Micron, v. 42, n. 5, p. 412–8, https://doi.org/10.1016/j.micron.2010.12.002

Berg, S., Ott, H., Klapp, S. A., Schwing, A., Neiteler, R., Brussee, N., Makurat, A., Leu, L., Enzmann, F., Schwarz, J. O., Kersten, M., Irvine, S., and Stampanoni, M., 2013, Real-time 3D imaging of Haines jumps in porous media flow: Proceedings of the National Academy of Sciences of the United States of America, v. 110, n. 10, p. 3755–9, https://doi.org/10.1073/pnas.1221373110

Berkowitz, B., Dror, I., Hansen, S. K., and Scher, H., 2016, Measurements and models of reactive transport in geological media: Reviews of Geophysics, v. 54, n. 4, p. 930–986, https://doi.org/10.1002/2016RG000524

Bi, L., Qin, G., Popov, P., Efendiev, Y., and Espadal, M. S., 2009, An Efficient Upscaling Process Based on a Unified Fine-scale Multi-Physics Model for Flow Simulation in Naturally Fracture Carbonate Karst Reservoirs: SPE/EAGE Reservoir Characterization and Simulation Conference, Abu Dhabi, UAE, SPE 125593, https://doi.org/10.2118/125593-MS

Bibi, I., Arvidson, R. S., Fischer, C., and Lüttge, A., 2018, Temporal Evolution of Calcite Surface Dissolution Kinetics: Minerals, v. 8, n. 6, p. 256, https://doi.org/10.3390/min8060256

Bollermann, T., and Fischer, C., 2020, Temporal evolution of dissolution kinetics of polycrystalline calcite: American Journal of Science, v. 320, n. 1, https://doi.org/10.2475/01.2020.04

Bouissonnié, A., Daval, D., Marinoni, M., and Ackerer, P., 2018, From mixed flow reactor to column experiments and modeling: Upscaling of calcite dissolution rate: Chemical Geology, v. 487, p. 63–75, https://doi.org/10.1016/j.chemgeo.2018.04.017

Brand, A. S., Feng, P., and Bullard, J. W., 2017, Calcite dissolution rate spectra measured by *in situ* digital holographic microscopy: Geochimica et Cosmochimica Acta, v. 213, p. 317–329, https://doi.org/10.1016/j.gca.2017.07.001

Brinkmann, H. C., 1947, A calculation of the viscous force exerted by a flowing fluid on a dense swarm of particles: Journal of Applied Sciences Research, v. 1, p. 27–34.

Bultreys, T., Boone, M. A., Boone, M. N., De Schryver, T., Masschaele, B., Van Hoorebeke, L., and Cnudde, V., 2016, Fast laboratory-based micro-computed tomography for pore-scale research: Illustrative experiments and perspectives on the future: Advances in Water Resources, v. 95, p. 341–351, https://doi.org/10.1016/j.advwatres.2015.05.012

Busenberg, E., and Plummer, L. N., 1986, A comparative study of the dissolution and crystal growth kinetics of calcite and aragonite, *in* Mumpton, F. A., editor, Studies in Diagenesis: U. S. Geological Survey Bulletin, v. 1587, p. 139–168.

Chou, L., Garrels, R. M., and Wollast, R., 1989, Comparative study of the kinetics and mechanisms of dissolution of carbonate minerals: Chemical Geology, v. 78, n. 3–4, p. 269–282, https://doi.org/10.1016/0009-2541(89)90063-6

Daval, D., Hellmann, R., Saldi, G. D., Wirth, R., and Knauss, K. G., 2013, Linking nm-scale Measurements of the Anisotropy of Silicate Surface Reactivity to Macroscopic Dissolution Rate Laws: New Insights Based on Diopside: Geochimica et Cosmochimica Acta, v. 107, p. 121–134, https://doi.org/10.1016/j.gca.2012.12.045

Deng, H., Molins, S., Trebotich, D., Steefel, C., and DePaolo, D., 2018, Pore-scale numerical investigation of the impacts of surface roughness: Upscaling of reaction rates in rough fractures: Geochimica et Cosmochimica Acta, v. 239, p. 374–389, https://doi.org/10.1016/j.gca.2018.08.005

Dentz, M., Le Borgne, T., Englert, A., and Bijeljic, B., 2011, Mixing, spreading and reaction in heterogeneous media: A brief review: Journal of Contaminant Hydrology, v. 120–121, p. 1–17, https://doi.org/10.1016/j.jconhyd.2010.05.002

Emmanuel, S., and Levenson, Y., 2014, Limestone weathering rates accelerated by micron-scale grain detachment: Geology, v. 42, n. 9, p. 751–754, https://doi.org/10.1130/G35815.1

Feldkamp, L. A., Davis, L. C., and Kress, J. W., 1984, Practical cone-beam algorithm: Journal of the Optical Society of America a-Optics Image Science and Vision, v. 1, n. 6, p. 612–619, https://doi.org/10.1364/JOSAA.1.000612

Fischer, C., and Luttge, A., 2017, Beyond the conventional understanding of water–rock reactivity: Earth and Planetary Science Letters, v. 457, p. 100–105, https://doi.org/10.1016/j.epsl.2016.10.019

——— 2018, Pulsating dissolution of crystalline matter: Proceedings of the National Academy of Sciences of the United States of America, v. 115, n. 5, p. 897–902, https://doi.org/10.1073/pnas.1711254115

Fischer, C., Arvidson, R. S., and Lüttge, A., 2012a, How predictable are dissolution rates of crystalline material?: Geochimica et Cosmochimica Acta, v. 98, p. 177–185, https://doi.org/10.1016/j.gca.2012.09.011

Fischer, C., Michler, A., Darbha, G. K., Kanbach, M., and Schäfer, T., 2012b, Deposition of mineral colloids onto rough rock surfaces: American Journal of Science, v. 312, n. 2, p. 885–906, https://doi.org/10.2475/08.2012.02

Fischer, C., Kurganskaya, I., Schäfer, T., and Lüttge, A., 2014, Variability of crystal surface reactivity: What do we know?: Applied Geochemistry, v. 43, p. 132–157, https://doi.org/10.1016/j.apgeochem.2014.02.002

Fischer, C., Kurganskaya, I., and Luttge, A., 2018, Inherited control of crystal surface: Applied Geochemistry, v. 91, p. 140–148, https://doi.org/10.1016/j.apgeochem.2018.02.003

Flukiger, F., and Bernard, D., 2009, A new numerical model for pore scale dissolution of calcite due to CO_2

saturated water flow in 3D realistic geometry: Principles and first results: Chemical Geology, v. 265, n. 1–2, p. 171–180, https://doi.org/10.1016/j.chemgeo.2009.05.004
Fritsch, W., 1953, Die Gumpeneckmarmore: Mitteilungen der Abteilung Geologie Paläontologie und Bergbau am Joanneum, v. 10, p. 3–12.
Godinho, J. R. A., and Withers, P. J., 2018, Time-lapse 3D imaging of calcite precipitation in a microporous column: Geochimica et Cosmochimica Acta, v. 222, p. 156–170, https://doi.org/10.1016/j.gca.2017.10.024
Godinho, J. R. A., Piazolo, S., and Evins, L. Z., 2012, Effect of surface orientation on dissolution rates and topography of CaF_2: Geochimica et Cosmochimica Acta, v. 86, p. 392–403, https://doi.org/10.1016/j.gca.2012.02.032
Godinho, J. R. A., Piazolo, S., and Evans, L., 2014, Simulation of surface dynamics during dissolution as a function of the surface orientation: Implications for non-constant dissolution rates: Earth and Planetary Science Letters, v. 408, p. 163–170, https://doi.org/10.1016/j.epsl.2014.10.018
Gouze, P., and Luquot, L., 2011, X-ray microtomography characterization of porosity, permeability and reactive surface changes during dissolution: Journal of Contaminant Hydrology, v. 120–121, p. 45–55, https://doi.org/10.1016/j.jconhyd.2010.07.004
Harries, D., Pollok, K., and Langenhorst, F., 2013, Oxidative dissolution of 4C- and NC-pyrrhotite: Intrinsic reactivity differences, pH dependence, and the effect of anisotropy: Geochimica et Cosmochimica Acta, v. 102, p. 23–44, https://doi.org/10.1016/j.gca.2012.10.021
Hellmann, R., Cotte, S., Cadel, E., Malladi, S., Karlsson, L. S., Lozano-Perez, S., Cabié, M., and Seyeux, A., 2015, Nanometre-scale evidence for interfacial dissolution–reprecipitation control of silicate glass corrosion: Nature Materials, v. 14, p. 307–311, https://doi.org/10.1038/nmat4172
Hemes, S., Desbois, G., Urai, J. L., Schröppel, B., and Schwarz, J.-O., 2015, Multi-scale characterization of porosity in Boom Clay (HADES-level, Mol, Belgium) using a combination of X-ray μ-CT, 2D BIB-SEM and FIB-SEM tomography: Microporous and Mesoporous Materials, v. 208, p. 1–20, https://doi.org/10.1016/j.micromeso.2015.01.022
Hiller, J., and Hornberger, P., 2016, Measurement accuracy in X-ray computed tomography metrology: Toward a systematic analysis of interference effects in tomographic imaging: Precision Engineering, v. 45, p. 18–32, https://doi.org/10.1016/j.precisioneng.2015.12.003
Kahl, W.-A., Hansen, C., and Bach, W., 2016, A new X-ray-transparent flow-through reaction cell for a μ-CT-based concomitant surveillance of the reaction progress of hydrothermal mineral-fluid interactions: Solid Earth, v. 7, p. 651–658, https://doi.org/10.5194/se-7-651-2016
Kulenkampff, J., Stoll, M., Gründig, M., Mansel, A., Lippmann-Pipke, J., and Kersten, M., 2018, Time-lapse 3D imaging by positron emission tomography of Cu mobilized in a soil column by the herbicide MCPA: Scientific Reports, v. 8, article number 7091, https://doi.org/10.1038/s41598-018-25413-9
Kurganskaya, I., and Churakov, S. V., 2018, Carbonate dissolution mechanisms in the presence of electrolytes revealed by grand canonical and kinetic Monte Carlo Modeling: The Journal of Physical Chemistry C, v. 122, n. 51, p. 29285–29297, https://doi.org/10.1021/acs.jpcc.8b08986
Kurganskaya, I., and Luttge, A., 2016, Kinetic Monte Carlo approach to study carbonate dissolution: The Journal of Physical Chemistry C, v. 120, n. 12, p. 6482–6492, https://doi.org/10.1021/acs.jpcc.5b10995
Lasaga, A. C., and Luttge, A., 2001, Variation of crystal dissolution rate based on a dissolution stepwave model: Science, v. 291, n. 5512, p. 2400–2404, https://doi.org/10.1126/science.1058173
Li, L., Steefel, C. I., and Yang, L., 2008, Scale dependence of mineral dissolution rates within single pores and fractures: Geochimica et Cosmochimica Acta, v. 72, n. 2, p. 360–377, https://doi.org/10.1016/j.gca.2007.10.027
Li, L., Maher, K., Navarre-Sitchler, A., Druhan, J., Meile, C., Lawrence, C., Moore, J., Perdrial, J., Sullivan, P., Thompson, A., Jin, L., Bolton, E. W., Brantley, S. L., Dietrich, W. E., Mayer, K. U., Steefel, C. I., Valocchi, A., Zachara, J., Kocar, B., McIntosh, J., Tutolo, B. M., Kumar, M., Sonnenthal, E., Bao, C., and Beisman, J., 2017, Expanding the role of reactive transport models in critical zone processes: Earth-Science Reviews, v. 165, p. 280–301, https://doi.org/10.1016/j.earscirev.2016.09.001
Li, X., Peterson, T. E., Gore, J. C., and Dawant, B. M., 2006, Automatic registration of whole body serial micro CT images with a combination of point-based and intensity-based registration techniques: 2006 3rd IEEE International Symposium on Biomedical Imaging: Macro to Nano, v. 1–3, p. 454–+. https://doi.org/10.1109/ISBI.2006.1624951
Liang, Y., and Baer, D. R., 1997, Anisotropic dissolution at the $CaCO_3$ water interface: Surface Science, v. 373, n. 2–3, p. 275–287, https://doi.org/10.1016/S0039-6028(96)01155-7
Liang, Y., Baer, D. R., McCoy, J. M., Amonette, J. E., and LaFemina, J. P., 1996, Dissolution kinetics at the calcite-water interface: Geochimica et Cosmochimica Acta, v. 60, p. 4883–4887, https://doi.org/10.1016/S0016-7037(96)00337-7
Luquot, L., and Gouze, P., 2009, Experimental determination of porosity and permeability changes induced by injection of CO_2 into carbonate rocks: Chemical Geology, v. 265, n. 1–2, p. 148–159, https://doi.org/10.1016/j.chemgeo.2009.03.028
Luttge, A., Fischer, C., Zhang, L., and Arvidson, R. S., 2007, Kink sites: A key to surface reactivity and dissolution kinetics: Geochimica et Cosmochimica Acta, v. 71, n. 15, Supplement, p. A603–A603, https://doi.org/10.1016/j.gca.2007.06.020
Luttge, A., Arvidson, R. S., and Fischer, C., 2013, Fundamental Controls of Dissolution Rate Spectra: Comparisons of Model and Experimental Results: Procedia Earth and Planetary Science, v. 7, p. 537–540, https://doi.org/10.1016/j.proeps.2013.03.115
Mahan, J. E., 2000, Physical vapor deposition of thin films: New York, Wiley-Interscience, 336 p.
Martys, N. S., Bentz, D. P., and Garboczi, E. J., 1994, Computer simulation study of the effective viscosity in Brinkman's equation: Physics of Fluids, v. 6, n. 4, p. 1434–1439, https://doi.org/10.1063/1.868258
Menke, H. P., Bijeljic, B., Andrew, M. G., and Blunt, M. J., 2015, Dynamic three-dimensional pore-scale

imaging of reaction in a carbonate at reservoir conditions: Environmental Science & Technology, v. 49, n. 7, p. 4407–4414, https://doi.org/10.1021/es505789f

Menke, H. P., Reynolds, C. A., Andrew, M. G., Nunes, J. P. P., Bijeljic, B., and Blunt, M. J., 2018, 4D multi-scale imaging of reactive flow in carbonates: Assessing the impact of heterogeneity on dissolution regimes using streamlines at multiple length scales: Chemical Geology, v. 481, p. 27–37, https://doi.org/10.1016/j.chemgeo.2018.01.016

Molins, S., 2015, Reactive interfaces in direct numerical simulation of pore scale processes: Reviews in Mineralogy and Geochemistry, v. 80, p. 461–481, https://doi.org/10.2138/rmg.2015.80.14

Molins, S., Trebotich, D., Steefel, C. I., and Shen, C., 2012, An investigation of the effect of pore scale flow on average geochemical reaction rates using direct numerical simulation: Water Resources Research, v. 48, n. 3, https://doi.org/10.1029/2011WR011404

Molins, S., Trebotich, D., Yang, L., Ajo-Franklin, J. B., Ligocki, T. J., Shen, C., and Steefel, C. I., 2014, Pore-Scale Controls on Calcite Dissolution Rates from Flow-through Laboratory and Numerical Experiments: Environmental Science & Technology, v. 48, n. 13, p. 7453–7460, https://doi.org/10.1021/es5013438

Moroni, G., and Petrò, S., 2016, Impact of the threshold on the performance verification of computerized tomography scanners: Procedia CIRP, v. 43, p. 345–350, https://doi.org/10.1016/j.procir.2016.02.082

——— 2018, A discussion on performance verification of 3d x-ray computed tomography systems: Procedia CIRP, v. 75, p. 125–130, https://doi.org/10.1016/j.procir.2018.04.064

Morse, J. W., and Arvidson, R. S., 2002, The dissolution kinetics of major sedimentary carbonate minerals: Earth-Science Reviews, v. 58, n. 1–2, p. 51–84, https://doi.org/10.1016/S0012-8252(01)00083-6

Noiriel, C., and Daval, D., 2017, Pore-Scale geochemical reactivity associated with CO_2 storage: New frontiers at the fluid–solid interface: Accounts of Chemical Research, v. 50, n. 4, p. 759–768, https://doi.org/10.1021/acs.accounts.7b00019

Noiriel, C., and Deng, H., 2018, Evolution of planar fractures in limestone: The role of flow rate, mineral heterogeneity and local transport processes: Chemical Geology, v. 497, p. 100–114, https://doi.org/10.1016/j.chemgeo.2018.08.026

Noiriel, C., Bernard, D., Gouze, P., and Thibault, X., 2005, Hydraulic properties and microgeometry evolution accompanying limestone dissolution by acidic water: Oil & Gas Science and Technology-Revue D Ifp Energies Nouvelles, v. 60, n. 1, p. 177–192, https://doi.org/10.2516/ogst:2005011

Noiriel, C., Luquot, L., Madé, B., Raimbault, L., Gouze, P., and van der Lee, J., 2009, Changes in reactive surface area during limestone dissolution: An experimental and modelling study: Chemical Geology, v. 265, n. 1–2, p. 160–170, https://doi.org/10.1016/j.chemgeo.2009.01.032

Noiriel, C., Oursin, M., Saldi, G., and Haberthür, D., 2019, Direct Determination of Dissolution Rates at Crystal Surfaces Using 3D X-ray Microtomography: ACS Earth and Space Chemistry, v. 3, n. 1, p. 100–108, https://doi.org/10.1021/acsearthspacechem.8b00143

Pereira Nunes, J. P., Bijeljic, B., and Blunt, M. J., 2016a, Pore-space structure and average dissolution rates: A simulation study: Water Resources Research, v. 52, n. 9, p. 7198–7212, https://doi.org/10.1002/2016WR019313

Pereira Nunes, J. P., Blunt, M. J., and Bijeljic, B., 2016b, Pore-scale simulation of carbonate dissolution in micro-CT images: Journal of Geophysical Research-Solid Earth, v. 121, n. 2, p. 558–576, https://doi.org/10.1002/2015JB012117

Peuble, S., Andreani, M., Gouze, P., Pollet-Villard, M., Reynard, B., and Van de Moortele, B., 2018, Multi-scale characterization of the incipient carbonation of peridotite: Chemical Geology, v. 476, p. 150–160, https://doi.org/10.1016/j.chemgeo.2017.11.013

Pollet-Villard, M., Daval, D., Ackerer, P., Saldi, G. D., Wild, B., Knauss, K. G., and Fritz, B., 2016a, Does crystallographic anisotropy prevent the conventional treatment of aqueous mineral reactivity? A case study based on K-feldspar dissolution kinetics: Geochimica et Cosmochimica Acta, v. 190, p. 294–308, https://doi.org/10.1016/j.gca.2016.07.007

Pollet-Villard, M., Daval, D., Fritz, B., Knauss, K. G., Schäfer, G., and Ackerer, P., 2016b, Influence of etch pit development on the surface area and dissolution kinetics of the orthoclase (001) surface: Chemical Geology, v. 447, p. 79–92, https://doi.org/10.1016/j.chemgeo.2016.09.038

Popov, P., Qin, G., Bi, L., Efendiev, Y., Kang, Z., and Li, J., 2009, Multiphysics and multiscale methods for modeling fluid flow through naturally fractured carbonate karst reservoirs: SPE Reservoir Evaluation & Engineering, v. 12, n. 2, p. 218–231, https://doi.org/10.2118/105378-PA

Qin, G., Bi, L., Popov, P., Efendiev, Y., and Espadal, M. S., 2010 of Conference, An efficient upscaling process based on a unified fine-scale multi-physics model for flow simulation in naturally fracture carbonate karst reservoirs: Beijing, China, International Oil and Gas Conference and Exhibition in China, Paper SPE 132236.

Saldi, G. D., Voltolini, M., and Knauss, K. G., 2017, Effects of surface orientation, fluid chemistry and mechanical polishing on the variability of dolomite dissolution rates: Geochimica et Cosmochimica Acta, v. 206, p. 94–111, https://doi.org/10.1016/j.gca.2017.02.007

Schott, J., Brantley, S., Crerar, D., Guy, C., Borcsik, M., and Willaime, C., 1989, Dissolution Kinetics of Strained Calcite: Geochimica et Cosmochimica Acta, v. 53, p. 373–382, https://doi.org/10.1016/0016-7037(89)90389-X

Sell, K., Enzmann, F., Kersten, M., and Spangenberg, E., 2013, Microtomographic quantification of hydraulic clay mineral displacement effects during a CO2 sequestration experiment with saline aquifer sandstone: Environmental Science & Technology, v. 47, n. 1, p. 198–204, https://doi.org/10.1021/es3013358

Sjoberg, E. L., 1978, Kinetics and mechanism of calcite dissolution in aqueous solutions at low temperatures: Stockholm Contributions in Geology, v. 32, n. 1, p. 1–92.

Smith, M. E., Knauss, K. G., and Higgins, S. R., 2013a, Effects of crystal orientation on the dissolution of

calcite by chemical and microscopic analysis: Chemical Geology, v. 360–361, p. 10–21, https://doi.org/10.1016/j.chemgeo.2013.09.015
Smith, M. M., Sholokhova, Y., Hao, Y., and Carroll, S. A., 2013b, CO_2-induced dissolution of low permeability carbonates. Part I: Characterization and experiments: Advances in Water Resources, v. 62, Part C, p. 370–387, https://doi.org/10.1016/j.advwatres.2013.09.008
——— 2013c, Evaporite Caprock Integrity: An Experimental Study of Reactive Mineralogy and Pore-Scale Heterogeneity during Brine-CO_2 Exposure: Environmental Science & Technology, v. 47, n. 1, p. 262–268, https://doi.org/10.1021/es3012723
Steefel, C. I., and Lasaga, A. C., 1994, A coupled model for transport of multiple chemical species and kinetic precipitation/dissolution reactions with application to reactive flow in single phase hydrothermal systems: American Journal of Science, v. 294, n. 5, p. 529–592, https://doi.org/10.2475/ajs.294.5.529
Steefel, C. I., Appelo, C. A. J., Arora, B., Jacques, D., Kalbacher, T., Kolditz, O., Lagneau, V., Lichtner, P. C., Mayer, K. U., Meeussen, J. C. L., Molins, S., Moulton, D., Shao, H., Šimůnek, J., Spycher, N., Yabusaki, S. B., and Yeh, G. T., 2015a, Reactive transport codes for subsurface environmental simulation: Computational Geosciences, v. 19, p. 445–478, https://doi.org/10.1007/s10596-014-9443-x
Steefel, C. I., Beckingham, L. E., and Landrot, G., 2015b, Micro-continuum approaches for modeling pore-scale geochemical processes: Reviews in Mineralogy and Geochemistry, v. 80, n. 1, p. 217–246, https://doi.org/10.2138/rmg.2015.80.07
Tartakovsky, D. M., Dentz, M., and Lichtner, P. C., 2009, Probability density functions for advective-reactive transport with uncertain reaction rates: Water Resources Research, v. 45, n. 7, https://doi.org/10.1029/2008WR007383
Thomas, T. R., 1999, Rough Surfaces: London, England, Imperial College Press, 278 p.
Tournassat, C., and Steefel, C. I., 2019, Reactive Transport Modeling of Coupled Processes in Nanoporous Media: Reviews in Mineralogy and Geochemistry, v. 85, p. 75–109, https://doi.org/10.2138/rmg.2019.85.4
Vialle, S., Contraires, S., Zinzsner, B., Clavaud, J. B., Mahiouz, K., Zuddas, P., and Zamora, M., 2014, Percolation of CO_2-rich fluids in a limestone sample: Evolution of hydraulic, electrical, chemical, and structural properties: Journal of Geophysical Research-Solid Earth, v. 119, n. 4, p. 2828–2847, https://doi.org/10.1002/2013JB010656
Villarraga-Gómez, H., Lee, C., and Smith, S. T., 2018, Dimensional metrology with X-ray CT: A comparison with CMM measurements on internal features and compliant structures: Precision Engineering, v. 51, p. 291–307, https://doi.org/10.1016/j.precisioneng.2017.08.021
Wang, Y., Zhang, L., Soong, Y., Dilmore, R., Liu, H., Lei, H., and Li, X., 2019, From core-scale experiment to reservoir-scale modeling: A scale-up approach to investigate reaction-induced permeability evolution of CO_2 storage reservoir and caprock at a U.S. CO_2 storage site: Computers & Geosciences, v. 125, p. 55–68, https://doi.org/10.1016/j.cageo.2019.01.006
Wild, B., Daval, D., Guyot, F., Knauss, K. G., Pollet-Villard, M., and Imfeld, G., 2016, pH-dependent control of feldspar dissolution rate by altered surface layers: Chemical Geology, v. 442, p. 148–159, https://doi.org/10.1016/j.chemgeo.2016.08.035
Yuan, K., Starchenko, V., Lee, S. S., De Andrade, V., Gursoy, D., Sturchio, N. C., and Fenter, P., 2019a, Mapping three-dimensional dissolution rates of calcite microcrystals: Effects of surface curvature and dissolved metal ions: ACS Earth and Space Chemistry, v. 3, n. 5, p. 833–843, https://doi.org/10.1021/acsearthspacechem.9b00003
Yuan, T., Ning, Y., and Qin, G., 2016, Numerical modeling and simulation of coupled processes of mineral dissolution and fluid flow in fractured carbonate formations: Transport in Porous Media, v. 114, p. 747–775, https://doi.org/10.1007/s11242-016-0742-7
——— 2017, Numerical modeling of mineral dissolution of carbonate rocks during geological co_2 sequestration processes: Society of Petroleum Engineers, 79th EAGE Conference and Exhibition, Paris, France, SPE-185845-MS, https://doi.org/10.2118/185845-MS
Yuan, T., Wei, C., Zhang, C. S., and Qin, G., 2019b, A Numerical Simulator for Modeling the Coupling Processes of Subsurface Fluid Flow and Reactive Transport Processes in Fractured Carbonate Rocks: Water, v. 11, n. 10, https://doi.org/10.3390/w11101957
Zednicek, W., 1983, Auflicht- und rasterelektronenmikroskopische Studie an einem Sölker Marmorblock: Mitteilungen der Abteilung für Mineralogie am Landesmuseum Joanneum, v. 51, p. 11–20.
Zeisig, A., Siegesmund, S., and Weiss, T., 2002, Thermal expansion and its control on the durability of marbles: Geological Society, London, Special Publications, v. 205, p. 65–80, https://doi.org/10.1144/GSL.SP.2002.205.01.06